



HAL
open science

A novel modal expansion method for low-order modeling of thermoacoustic instabilities in complex geometries

Charl lie Laurent, Micha l Bauerheim, Thierry Poinsot, Franck Nicoud

► To cite this version:

Charl lie Laurent, Micha l Bauerheim, Thierry Poinsot, Franck Nicoud. A novel modal expansion method for low-order modeling of thermoacoustic instabilities in complex geometries. *Combustion and Flame*, 2019, 206, pp.334-348. 10.1016/j.combustflame.2019.05.010 . hal-02164029

HAL Id: hal-02164029

<https://hal.science/hal-02164029>

Submitted on 24 Jun 2019

HAL is a multi-disciplinary open access archive for the deposit and dissemination of scientific research documents, whether they are published or not. The documents may come from teaching and research institutions in France or abroad, or from public or private research centers.

L'archive ouverte pluridisciplinaire **HAL**, est destin e au d p t et   la diffusion de documents scientifiques de niveau recherche, publi s ou non,  manant des  tablissements d'enseignement et de recherche fran ais ou  trangers, des laboratoires publics ou priv s.



Open Archive Toulouse Archive Ouverte (OATAO)

OATAO is an open access repository that collects the work of some Toulouse researchers and makes it freely available over the web where possible.

This is an author's version published in: <https://oatao.univ-toulouse.fr/23926>

Official URL : <https://doi.org/10.1016/j.combustflame.2019.05.010>

To cite this version :

Laurent, Charl lie and Bauerheim, Micha l and Poinso, Thierry and Nicoud, Franck A novel modal expansion method for low-order modeling of thermoacoustic instabilities in complex geometries. (2019) Combustion and Flame, 206. 334-348. ISSN 0010-2180

Any correspondence concerning this service should be sent to the repository administrator:

tech-oatao@listes-diff.inp-toulouse.fr

A novel modal expansion method for low-order modeling of thermoacoustic instabilities in complex geometries

C. Laurent^{a,*}, M. Bauerheim^{a,d}, T. Poinso^c, F. Nicoud^b

^aCERFACS, 42 Avenue Gaspard Coriolis, Toulouse Cedex 1 31057, France

^bCNRS, IMAG, Université de Montpellier, Montpellier, France

^cIMFT, Allée du Professeur Camille Soula, Toulouse 31400, France

^dISAE-Supaero, 10 Avenue Edouard-Belin, Toulouse Cedex 4 31055, France

A B S T R A C T

This work proposes an improvement to existing methods based on modal expansions used for the prediction of thermoacoustic instabilities in zero Mach number flow conditions. Whereas the orthogonal basis made of the acoustic eigenmodes of the domain bounded by rigid walls is classically used, an alternative method based on a modal expansion onto an over-complete set of acoustic eigenmodes is proposed. This allows avoiding the misrepresentation of the acoustic velocity field often observed near non rigid-wall boundaries. A Low Order Model network utilizing a state-space framework is then built upon this novel type of modal expansion. Several test cases, going from non reacting ducts to a complex geometry with combustion, are studied to assess the potential of the approach. The methodology not only successfully mitigates the misrepresentation in the acoustic field in the presence of non-rigid-wall boundaries, but it also drastically improves the convergence speed. The modularity of the method and its ability to handle complex geometries are illustrated by considering a configuration featuring an annular chamber, an annular plenum, as well as multiple burners. This novel technique is expected to bring worthy improvements to existing Low Order Models using modal expansions for the prediction of combustion instabilities.

Keywords:

Thermoacoustic instabilities

Low Order Model

Modal expansion

State-space

Acoustic network

1. Introduction

Since their early study by Rayleigh [1], thermoacoustic instabilities have been a subject of primary scientific interest as well as a major concern for a number of industrial projects. Experiments with increasingly complex setups and advanced diagnostics were carried out over the years to study this intricate interplay between flame dynamics and acoustic waves. Progresses in experimental works were accompanied by considerable efforts in both numerical and theoretical study of thermoacoustic instabilities. Regarding the former, Large Eddy Simulation (LES) was proved as the most accurate tool for the analysis of instabilities in combustors featuring complex geometries [2]. Yet, the high cost of these full scale simulations led to a growing popularity of alternative and cheaper numerical methods relying on a separation of the acoustic flow and the complex flame dynamics. The acoustic field is solution of the Helmholtz equation in the frequency domain, while the flame response to acoustic perturbations is often embedded into a

Flame Transfer Function (FTF) [3], or a Flame Describing Function (FDF) representing nonlinear effects [4].

One of the key aspects for the resolution of thermoacoustic eigenmodes is the ability of the method to accurately account for complex geometries that are encountered in industrial combustors. One of the most straightforward approaches is the direct discretization of the Helmholtz equation that is then solved thanks to a Finite Element Method (FEM) solver. State-of-the-art FEM Helmholtz solvers are able to solve for thermoacoustic eigenmodes in complex geometries comprising active flames and dissipative effects [5,6], and can also incorporate the FDF formalism to capture nonlinear limit-cycle behaviors [7,8]. However, direct discretization FEM Helmholtz solvers often result in a large number of Degrees of Freedom (DoF), synonym of a considerable computational cost, and only permit little modularity, as any change in the geometrical parameters requires a new geometry and mesh generation. In order to circumvent these shortcomings, numerous research groups have opted for the development of Low Order Models (LOMs) enabling even cheaper resolution of thermoacoustic instabilities. Low Order Modeling resides in two basic ideas: (1) the number of DoF should be reduced as much as possible in order to permit fast computations, and (2) the model should be flexible and highly modular, in the sense that it should allow for

* Corresponding author.

E-mail address: laurent@cerfacs.fr (C. Laurent).

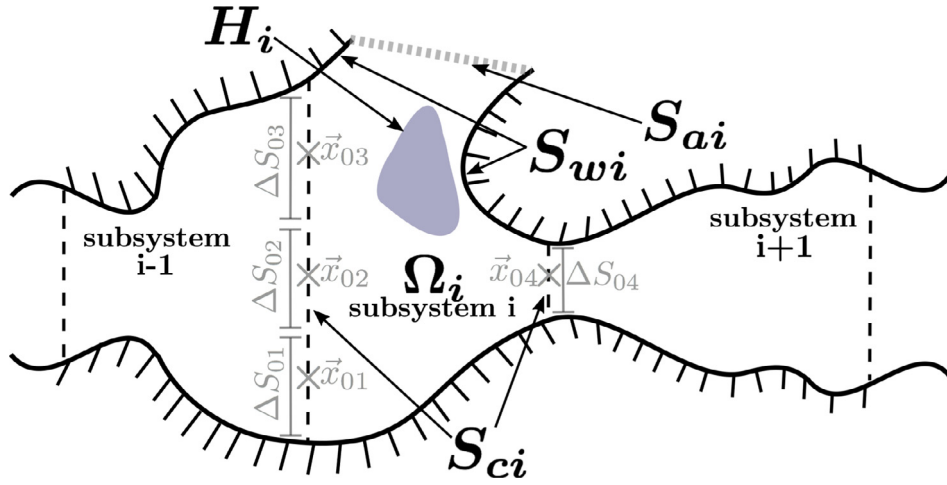


Fig. 1. Schematic representation of an acoustic network. Hashed lines show rigid walls. Gray dotted lines are opening to the atmosphere. The geometry is split into distinct subsystems, that are connected together. The subsystem (i) is defined by its volume Ω_i , its rigid wall boundary S_{wi} , its boundary opened to the atmosphere S_{ci} , and its boundaries S_{ci} that are to be connected to other subsystems in the acoustic network. The interface S_{ci} is split into several surface elements ΔS_{0j} located at the connection points \vec{x}_{0j} . It also contains a volume heat source H_i .

the straightforward modification of most geometrical or physical parameters. The latter point is often achieved thanks to a *divide and conquer* strategy, where complex geometries are decomposed into an acoustic network of simpler subdomains (see Fig. 1). Fast and modular LOMs have been promisingly applied to intensive tasks demanding a large number of repeated resolutions, such as Monte Carlo Uncertainty Quantification [9,10], or passive control through adjoint geometrical optimization [11].

Existing thermoacoustic LOMs can be classified into four main categories, according to the method employed to describe the acoustic field.

1. The first class of LOM is a wave-based 1D network approach, where the acoustic pressure and velocity are written in function of the Riemann invariants A^+ and A^- . This method was first successfully used in the LOTAN tool [12], designed to resolve in the frequency domain linearly unstable thermoacoustic modes in simple configurations. More recently and in a similar fashion, the open-source LOM solver Oscilos [13] developed at Imperial College, London, was used to perform for instance time-domain simulations of thermoacoustic limit cycles in longitudinal combustors [14,15] comparable to the Rijke tube [16]. Wave-based low order modeling was also generalized to more complex cases, including azimuthal modes in configurations comprising an annular combustion chamber linked to an annular plenum through multiple burners. This procedure allowed Bauerheim et al. to conduct a series of studies based on a family of analytical solutions for azimuthal modes in annular combustors [9,17,18]. Even though wave-based LOMs are the most adequate to deal with networks of longitudinal elements where acoustic waves can be assumed as planar, they also suffer strict limitations: they are indeed unable to capture non-planar modes in complex geometries.
2. The second class of LOM relies on modal (or Galerkin) expansions, to express the acoustic pressure field as a combination of known acoustic modes. Modal expansion was first introduced and formalized in an acoustic context by Morse and Ingard in their influential book *Theoretical Acoustics* [19] dated from 1968. In the field of thermoacoustics, Zinn et al. [20] and Culick [21–24] were among the first to use it to study combustion instabilities in liquid fuel rocket engines. Similarly to the wave-based approach, multiple studies utilizing modal expansions are dealing with the Rijke tube: for example by Ju-

- niper [25], Waugh and Juniper [26], and Balasubramanian and Sujith [27]. Simplified annular configurations were also examined thanks to pressure modal expansion: Noiray and co-workers [28–30] and Ghirardo et al. [31] conducted a series of theoretical studies in such geometries. More complex modal expansion-based networks were developed for multi-burners chamber-plenum geometries, by Stow and Dowling [32], Schuermans and co-workers [33,34], and Belluci et al. [35]. Their strategy is to perform modal expansions for the pressure in the chamber/plenum and to assume acoustically compact burners that can be lumped and represented by simple transfer matrices. Unlike wave-based low-order modeling, this method is not limited to planar acoustic waves, and can resolve both azimuthal and longitudinal chamber modes. Even though their approach does not rely on an acoustic network decomposition, Bethke et al. [36] showed that arbitrarily complex geometries can be incorporated in a thermoacoustic LOM by expanding the pressure onto a set of basis functions computed in a preliminary step thanks to a FEM Helmholtz solver. Although they appear more general than wave-based LOMs, modal expansion-based LOMs are also subjected to strict limitations, which mainly resides in the choice of the modal basis employed to expand the acoustic pressure. This point is the main object of this paper, and is discussed in more details later.
3. The third class of thermoacoustic LOM is a mixed method, that combines both Riemann invariants and modal expansions. The former are used to account for longitudinal propagation, while the latter are used to account for multi-dimensional geometries. This mixed method was employed by Evesque and Polifke [37] to model azimuthal modes in multi-burners annular chamber/plenum configurations. In more recent works [38,39] the mixed strategy was further developed to investigate nonlinear spinning/standing limit cycles in the MICCA annular combustor. More precisely, in [38] the planar acoustic field in the ducted burners is represented by Riemann invariants, while it is represented through modal expansions in the chamber and in the plenum.
 4. Finally, the last class of LOMs consists in those based on a direct spatial discretization. For example, Sayadi et al. [40] made use of a finite difference scheme to build a dynamical system representation of a one-dimensional thermoacoustic system comprising a volumetric heat source localized within the domain. A more generic direct discretization LOM is the taX

Low-Order Model developed at Technical University of Munich [41]. Its modularity lies in the ability to combine in a same thermoacoustic network one-dimensional elements discretized by finite difference, geometrically complex elements discretized through FEM, and other types of elements such as FTFs and scattering matrices. Since this LOM is built upon direct discretization of linearized partial differential equations, it can also potentially incorporate richer physics, including mean flow effects or acoustic–vortex interactions. However, the price to pay for this high modularity is a large number of DoF: for instance, in the taX LOM, about $O(10^5)$ DoF were needed to obtain acoustic eigenmodes of an annular combustor comprising 12 ducted injectors (but no active flame).

Interestingly, most modal expansion LOMs used the same type of eigenmodes basis, namely the basis composed of the *rigid-wall cavity modes*, or in other words acoustic eigenmodes satisfying homogeneous Neumann boundary conditions (*i.e.* zero normal velocity) over the entire boundaries of the domain (and without internal volume sources). This paper focuses on the nature of the acoustic eigenmodes basis used to decompose the pressure, and the convergence properties resulting from this expansion. Although the rigid-wall modal basis presents the huge advantage of being orthogonal, many actual systems obviously comprise frontiers with far more complex boundary conditions than just a homogeneous Neumann condition (for example an inlet or an outlet where the impedance has a finite value). The use of such basis then appears paradoxical: *how is it possible that a solution expressed as a rigid-wall modes series converges towards a solution satisfying a non rigid-wall boundary condition?* This singularity in the pressure modal expansion was already noticed by Morse and Ingard [19], but they did not study its impact on the convergence of the whole method. Later, Culick [24] provided more explanations about this singularity: the modal expansion does not converge uniformly over the domain, but only in the less restrictive sense of the Hilbert norm (L_2 norm); as a result, even though each individual term of the expansion does not satisfy the appropriate boundary condition, the infinite sum of these terms may satisfy it. In other words, “the limit of the sum is not equal to the sum of the limit” in the neighborhood of the boundary. An interesting examination regarding this singularity is provided in a recent work by Ghirardo et al. [42], where a projection onto a mode satisfying a specific non rigid-wall inlet boundary condition was discussed. The convergence issue arising from rigid-wall modal expansion is even more problematic in the case of acoustic LOMs where the geometry is decomposed into a network of subsystems that need to be coupled together at their boundaries (see Fig. 1). For each individual subdomain, these coupling boundaries are not rigid-wall but each term of the basis corresponds to a rigid-wall: the convergence singularity may arise at each one of the coupling interfaces. Although Culick [24] proposed an explanation to this singularity based on a *local* justification, only very few studies deal with *global* effects, such as for example convergence speed of the eigenfrequencies.

The main contribution of this work is a reformulation of the modal expansion method under the zero Mach number flow assumption, allowing for decompositions of the pressure onto an *over-complete family of modes*, gathering rigid-wall ($u' = 0$) and pressure release ($p' = 0$) modes, instead of the classical rigid-wall modes basis. This paper is organized as follows: in Section 2, the original mathematical derivation of pressure expansion onto the rigid-wall modal basis is recalled. The problem is then reformulated using expansions onto an over-complete set of modes, also called a *frame*. In this frame, non rigid-wall conditions are used for certain elements. Section 3 briefly describes the state-space formalism proposed in [33,34] to couple subsystems together and build a modular acoustic LOM network. This state-space formal-

ism is then extended to account for the *frame* of non-orthogonal modes. In Section 4, the convergence properties are evaluated and compared for both types of modal expansions on a canonical case which consists of a long duct with a sharp cross-section change. Finally in Section 5, the modularity of the proposed LOM and its ability to deal with cases involving combustion instabilities in complex configurations is demonstrated by considering an annular chamber/plenum configuration featuring multiple burners.

2. Acoustic pressure modal expansion

In acoustic LOM networks for complex configurations, the system is split into smaller geometric subsystems. Let us consider a subsystem (i) as in Fig. 1, defined as a bounded domain Ω_i delimited by $\partial\Omega_i = S_{wi} \cup S_{ai} \cup S_{ci}$. The primary variable of interest is the acoustic pressure $p(\vec{x}, t)$ expressed in the physical space, but its frequency-domain counterpart $\hat{p}(\vec{x}, \omega)$ is often introduced to ease the analysis, especially when dealing with linear acoustics. These two quantities are related by the (inverse) Fourier transform as follows:

$$\hat{p}(\vec{x}, \omega) = \int_{-\infty}^{+\infty} e^{-j\omega t} p(\vec{x}, t) dt, \quad p(\vec{x}, t) = \int_{-\infty}^{+\infty} e^{j\omega t} \hat{p}(\vec{x}, \omega) d\omega \quad (1)$$

For the sake of simplicity, in the following the sound speed field is assumed uniform and the baseline flow to be at rest. Note however that these hypotheses are not necessary and could be omitted. The frequency-domain acoustic pressure $\hat{p}(\vec{x}, \omega)$ in the subsystem Ω_i is then solution of the following Helmholtz equation:

$$\begin{cases} c_0^2 \nabla^2 \hat{p}(\vec{x}, \omega) - j\alpha\omega \hat{p}(\vec{x}, \omega) + \omega^2 \hat{p}(\vec{x}, \omega) = \hat{h}(\vec{x}, \omega) & \text{for } \vec{x} \in \Omega_i \\ \nabla_s \hat{p} = 0 & \text{for } \vec{x}_s \in S_{wi}, \quad \hat{p} = 0 & \text{for } \vec{x}_s \in S_{ai} \\ \nabla_s \hat{p} = \hat{f}(\vec{x}_s, \omega) & \text{for } \vec{x}_s \in S_{ci} \end{cases} \quad (2)$$

where the notation $\nabla_s \hat{p} = \vec{\nabla} \hat{p}(\vec{x}_s) \cdot \vec{n}_s$ is introduced, \vec{x}_s being a geometrical point belonging to a boundary of the flow domain and \vec{n}_s the normal unity vector pointing outward. In Eq. (2), α is an acoustic loss coefficient, the term $\hat{h}(\vec{x}, \omega)$ is a volume acoustic source, while $\hat{f}(\vec{x}, \omega)$ is a surface forcing term imposed on the connection boundary S_{ci} : it is an external input to the acoustic subsystem contained in Ω_i exerted by adjacent subsystems. The pressure verifies rigid-wall boundary condition on S_{wi} and is null on S_{ai} . The volumic source $\hat{h}(\vec{x}, \omega)$ represents fluctuations of heat release, and it may be written as follows:

$$\hat{h}(\vec{x}, \omega) = -j\omega(\gamma - 1)\hat{\omega}_T(\vec{x}, \omega) = -j\omega(\gamma - 1)\mathcal{H}_i(\vec{x})\hat{Q}(\omega) \quad (3)$$

where γ is the heat capacity ratio and $\hat{\omega}_T(\vec{x}, \omega)$ is the local fluctuating heat release rate resulting from flame dynamics. In Eq. (3), $\hat{\omega}_T(\vec{x}, \omega)$ is decomposed into a global heat release rate $\hat{Q}(\omega)$ and a spatial volume density $\mathcal{H}_i(\vec{x})$ representing the flame shape (the integral of $\mathcal{H}_i(\vec{x})$ over Ω_i is unity). In the following, only one flame in the subdomain Ω_i is considered for conciseness, but the reasoning can be extended without difficulty to any number of distinct and independent flames located in a same subdomain Ω_i .

In modal expansion based LOMs, on each subsystem Ω_i the pressure is decomposed onto a family formed of known acoustic eigenmodes of Ω_i . The purpose is then to derive a set of governing equations for the corresponding modal amplitudes. This step usually makes use of the inner product defined for any functions $f(\vec{x})$ and $g(\vec{x})$ as:

$$\langle f, g \rangle = \iiint_{\Omega} f(\vec{x})g(\vec{x}) d^3\vec{x} \quad (4)$$

The associated L^2 norm is noted $\|f\|_2 = \langle f, f \rangle^{1/2}$.

2.1. The classical rigid-wall modal expansion

The usual derivation consists in writing the decomposition of the acoustic pressure onto an orthogonal basis of known acoustic modes $(\psi_n(\vec{x}))_{n \geq 1}$ of the subdomain Ω_i , as $\hat{p}(\vec{x}, \omega) = \sum_n \hat{\gamma}_n(\omega) \psi_n(\vec{x})$. The set $(\psi_n(\vec{x}))_{n \geq 1}$ is classically chosen as the rigid-wall eigenmodes of the subsystem Ω_i (without volume sources and acoustic damping). These eigenmodes verify rigid-wall conditions (*i.e.* zero normal velocity) over S_{wi} , but also over the connection boundary S_{ci} . In the presence of boundaries that are known to be opened to the atmosphere (S_{ai} in Fig. 1), the eigenmodes basis can be chosen to satisfy the appropriate condition on S_{ai} (*i.e.* zero pressure), without further difficulty since the expansion basis is still orthogonal. The set $(\psi_n(\vec{x}))_{n \geq 1}$ is solution of the following eigenvalue problem:

$$\begin{cases} c_0^2 \nabla^2 \psi_n + \omega_n^2 \psi_n = 0 & \text{for } \vec{x} \in \Omega_i \\ \nabla_s \psi_n = 0 & \text{for } \vec{x} \in S_{wi}, \quad \psi_n = 0 & \text{for } \vec{x} \in S_{ai} \\ \nabla_s \psi_n = 0 & \text{for } \vec{x} \in S_{ci} \end{cases} \quad (5)$$

where ω_n is the eigen-pulsation of the n^{th} eigenmode. By making use of the second Green's identity (reminded in Supplemental Material A), it can be shown that the set $(\psi_n(\vec{x}))_{n \geq 1}$ defined by Eq. (5) is indeed an orthogonal basis, that is $\langle \psi_n, \psi_m \rangle = 0$ for any $n \neq m$.

For conciseness, the successive steps required to obtain the modal amplitudes $\hat{\gamma}_n(\omega)$ are not detailed here, but the interested reader is referred to Supplemental Material A, as well as [19,43]. To ease the formalism, the connection surface S_{ci} is split into M_S elements ΔS_{0j} connecting Ω_i with the adjacent subdomains Ω_j at the boundary points \vec{x}_{0j} . Note that the subdomains Ω_j are not necessarily distinct, since there may exist several connection points between Ω_i and a same neighbor (*i.e.* we can have $\vec{x}_{0j1} \neq \vec{x}_{0j2}$, but $\Omega_{j1} = \Omega_{j2}$). An example of such surface splitting is shown in Fig. 1. After projecting the pressure field onto the orthogonal basis $(\psi_n(\vec{x}))_{n \geq 1}$ thanks to the inner product defined in Eq. (4), the modal amplitudes $\hat{\gamma}_n(\omega)$ are found to be solutions of the following equation:

$$\begin{aligned} (\omega^2 - j\omega\alpha - \omega_n^2) \left(\frac{\hat{\gamma}_n(\omega)}{j\omega} \right) &= \sum_{j=1}^{M_S} \frac{\rho_0 c_0^2 \Delta S_{0j} \psi_n(\vec{x}_{0j})}{\Lambda_n} \hat{u}_s^{\Omega_j}(\vec{x}_{0j}, \omega) \\ &\quad - \frac{(\gamma - 1) \mathcal{H}_i^{(n)}}{\Lambda_n} \hat{Q}(\omega) \end{aligned} \quad (6)$$

where $\Lambda_n = \|\psi_n\|_2^2$, $\mathcal{H}_i^{(n)} = \langle \mathcal{H}_i, \psi_n \rangle$ is the projection of the flame shape $\mathcal{H}_i(\vec{x})$ onto $\psi_n(\vec{x})$, and $\hat{u}_s^{\Omega_j}(\vec{x}_{0j}, \omega) = -\hat{f}(\vec{x}_{0j}, \omega) / (\rho_0 j\omega)$ is the normal velocity forcing imposed by adjacent subsystems Ω_j at the boundary points \vec{x}_{0j} .

Since time derivative in the physical space corresponds to multiplying by $j\omega$ in the Fourier domain, it is possible to recast Eq. (6) into the time-domain. In doing so, it proves useful to introduce $\hat{\Gamma}_n = \hat{\gamma}_n / (j\omega)$ (*i.e.* $\hat{\Gamma}_n(t) = \gamma_n(t)$) and then use the inverse Fourier transform to obtain:

$$\begin{cases} p(\vec{x}, t) = \sum_{n=1}^{\infty} \hat{\Gamma}_n(t) \psi_n(\vec{x}) \\ \hat{\Gamma}_n(t) = -\alpha \hat{\Gamma}_n(t) - \omega_n^2 \Gamma_n(t) - \sum_{j=1}^{M_S} \frac{\rho_0 c_0^2 \Delta S_{0j} \psi_n(\vec{x}_{0j})}{\Lambda_n} u_s^{\Omega_j}(\vec{x}_{0j}, t) \\ \quad + \frac{(\gamma - 1) \mathcal{H}_i^{(n)}}{\Lambda_n} Q(t) \end{cases} \quad (7)$$

This dynamical system governs the temporal evolution of the pressure field in the subdomain Ω_i , under the normal velocity forcing $u_s^{\Omega_j}(\vec{x}_{0j}, t)$ imposed by adjacent subsystems Ω_j , and under the volume forcing $Q(t)$ imposed by fluctuating flames contained within Ω_i . This set of equations was used for example in [32,33], where the infinite series was truncated up to a finite order N . It is also worth noting that the acoustic velocity can be calculated from the knowledge of the modal amplitudes $\Gamma_n(t)$ as $\vec{u}(x, t) = -\sum_n \Gamma_n(t) \vec{\nabla} \psi_n(\vec{x}) / \rho_0$. A state-space approach can then be used to couple together the subsystems defining the whole thermoacoustic system of interest. This formalism will be detailed in Section 3.

Finally, since the acoustic pressure is a linear combination of the modal basis vectors ψ_n , it necessarily verifies the same boundary conditions, in particular $\nabla_s p = 0$, *viz.* $\vec{u} \cdot \vec{n}_s = 0$ on S_{ci} . Since the acoustic velocity should not be zero over the boundaries of the (arbitrarily chosen) sub-domain Ω_i , this may result in a singularity in the representation of the acoustic velocity field. The impact of this singularity on the convergence properties of the method is discussed in Section 4. The following section proposes a mathematical reformulation of the pressure modal expansion to mitigate this undesirable feature.

2.2. Modal expansion onto an over-complete frame of acoustic eigenmodes

The purpose is now to introduce a modal expansion of the acoustic pressure that would allow for satisfying any boundary condition on S_{ci} (and not $\nabla_s p = 0$ only). In this matter, it is necessary to retain in the modal expansion an additional degree of freedom, such that both acoustic pressure and normal acoustic velocity at the connection boundary S_{ci} remain *a priori* undetermined. Let us then introduce two distinct families $(\xi_m)_{m \geq 1}$ and $(\zeta_k)_{k \geq 1}$ of acoustic eigenmodes of the subsystem Ω_i , characterized by the two following eigenproblems:

$$\begin{cases} c_0^2 \nabla^2 \xi_m + \omega_m^2 \xi_m = 0 & \text{for } \vec{x} \in \Omega_i \\ \nabla_s \xi_m = 0 & \text{for } \vec{x} \in S_{wi}, \quad \xi_m = 0 & \text{for } \vec{x} \in S_{ai} \\ \nabla_s \xi_m = 0 & \text{for } \vec{x} \in S_{ci} \end{cases} \quad (8)$$

$$\begin{cases} c_0^2 \nabla^2 \zeta_k + \omega_k^2 \zeta_k = 0 & \text{for } \vec{x} \in \Omega_i \\ \nabla_s \zeta_k = 0 & \text{for } \vec{x} \in S_{wi}, \quad \zeta_k = 0 & \text{for } \vec{x} \in S_{ai} \\ \zeta_k = 0 & \text{for } \vec{x} \in S_{ci} \end{cases} \quad (9)$$

Both eigenmodes families $(\xi_m)_{m \geq 1}$ and $(\zeta_k)_{k \geq 1}$ verify the same rigid-wall (*resp.* open) boundary conditions on S_{wi} (*resp.* S_{ai}). The eigenmodes family $(\xi_m)_{m \geq 1}$ is similar to the orthogonal basis $(\psi_n)_{n \geq 1}$ used in Section 2.1. Conversely, the eigenmodes family $(\zeta_k)_{k \geq 1}$ differs since it verifies open boundary conditions on S_{ci} .

Consider now the eigenmodes family $(\phi_n)_{n \geq 1}$ formed as the concatenation of $(\xi_m)_{m \geq 1}$ and $(\zeta_k)_{k \geq 1}$: $(\phi_n)_{n \geq 1} = (\xi_m)_{m \geq 1} \cup (\zeta_k)_{k \geq 1}$. The eigenpulsations associated to the eigenmodes ϕ_n are noted $(\omega_n)_{n \geq 1} = (\omega_m)_{m \geq 1} \cup (\omega_k)_{k \geq 1}$. As a concatenation of two orthogonal bases, $(\phi_n)_{n \geq 1}$ is not a basis but is instead an over-complete set of eigenmodes, also called a *frame* [44]. The concept of frame was introduced in the context of nonharmonic Fourier analysis [45], and later used in a number of fields ranging from wavelet analysis, to digital image processing and time-series forecasting. The use of an over-complete frame to perform modal expansions is the most crucial element of the proposed method. Let us precise that the frame $(\phi_n)_{n \geq 1}$ could be built from the concatenation of other sets of eigenmodes, as long as those do not *a priori* impose any constraint between pressure and velocity at the boundary S_{ci} . However, using the concatenation of the rigid-wall basis $(\xi_m)_{m \geq 1}$ and the open atmosphere basis $(\zeta_k)_{k \geq 1}$ has two main advantages: (1) they are usually the easiest to obtain analytically or

numerically, and (2) the frame $(\phi_n)_{n \geq 1}$ formed by their concatenation verifies a generalized Perseval's identity which ensures the well-posedness of modal expansions [44].

In the following, a compact vectorial notation is introduced to avoid the use of multiple summation symbols: for any indexed quantity $(f_i)_{i \geq 1}$ we note \underline{f} the column-vector such that: ${}^t \underline{f} = (f_0 \ f_1 \ f_2 \ \dots)$, where ${}^t(\cdot)$ designates the vector transpose. For a doubly indexed quantity $(f_{ij})_{i,j \geq 1}$, we note $\underline{\underline{f}}$ the matrix whose coefficients are the f_{ij} . Conversely, $(\underline{f})_n$ is the n^{th} component of the vector \underline{f} . Similarly to Section 2.1, the pressure modal expansion is sought under the form $\hat{p}(\vec{x}, \omega) = \sum_n \hat{\gamma}_n(\omega) \phi_n(\vec{x})$, that is, using the vectorial notation $\hat{p}(\vec{x}, \omega) = {}^t \hat{\gamma}(\omega) \underline{\underline{\phi}}(\vec{x})$. The analytical derivation of the modal amplitudes $\hat{\gamma}_n(\omega)$ is rather long and its details are not necessary to understand the remaining of the paper; it is thus not included here but made available in Supplemental Material B. As an outcome of this analytical derivation, the modal amplitudes $\hat{\gamma}_n(\omega)$ are found to be solutions of the following equation:

$$\begin{aligned} (\omega^2 - j\omega\alpha - \omega_n^2) \left(\frac{\hat{\gamma}_n(\omega)}{j\omega} \right) &= \sum_{j=1}^{M_s} \rho_0 c_0^2 \phi_n^\perp(\vec{x}_{0j}) \hat{u}_s^{\Omega_j}(\vec{x}_{0j}) \\ &\quad - \sum_{j=1}^{M_s} \rho_0 c_0^2 \nabla_s \phi_n^\perp(\vec{x}_{0j}) \hat{\varphi}^{\Omega_j}(\vec{x}_{0j}) \\ &\quad - (\gamma - 1) \mathcal{H}_{i,n}^\perp \hat{Q}(\omega) \end{aligned} \quad (10)$$

where:

$$\begin{aligned} \phi_n^\perp(\vec{x}_{0j}) &= \Delta S_{0j} (\underline{\underline{\Delta}}^{-1} \underline{\underline{\phi}}(\vec{x}_{0j}))_n, \quad \nabla_s \phi_n^\perp(\vec{x}_{0j}) = \Delta S_{0j} (\underline{\underline{\Delta}}^{-1} \underline{\underline{\nabla}}_s \underline{\underline{\phi}}(\vec{x}_{0j}))_n, \\ \mathcal{H}_{i,n}^\perp &= (\underline{\underline{\Delta}}^{-1} \underline{\underline{\mathcal{H}}}_i)_n \end{aligned} \quad (11)$$

As previously the surface S_{ci} has been decomposed into M_s plane surface elements ΔS_{0j} located at \vec{x}_{0j} . In Eq. (11), $\underline{\underline{\Delta}} = \langle {}^t \underline{\underline{\phi}}, \underline{\underline{\phi}} \rangle$ is the matrix whose coefficients are $\Delta_{mn} = \langle \phi_m, \phi_n \rangle$. This matrix is the Gram matrix associated to the over-complete frame $(\phi_n)_{n \geq 1}$: it reduces to a diagonal matrix in the case of an orthogonal basis. The volume source $\hat{h}(\vec{x}, \omega)$ is expressed according to Eq. (3), and \mathcal{H}_i is the column vector containing all the projections of the flame shape $\mathcal{H}_i(\vec{x})$ onto the elements of the over-complete frame $(\phi_n(\vec{x}))_{n \geq 1}$. In Eq. (10), $\hat{u}_s^{\Omega_j}(\vec{x}_{0j})$ is the velocity forcing imposed onto Ω_i by the adjacent subsystems Ω_j at the connection points \vec{x}_{0j} , while $\hat{\varphi}^{\Omega_j}(\vec{x}_{0j}) = -\hat{p}^{\Omega_j}(\vec{x}_{0j})/(\rho_0 j\omega)$ is an acoustic potential forcing imposed onto Ω_i at these boundary points. One may note that the second term in the right-hand side of Eq. (10) has no counterpart in Eq. (6), contrary to the first and third terms.

As in Section 2.1 for Eq. (6), Eq. (10) can then be recast into the time-domain by introducing $\Gamma_n(t)$ such that $\gamma_n(t) = \Gamma_n(t)$; this leads to:

$$\begin{cases} p(\vec{x}, t) = \sum_{n=1}^N \dot{\Gamma}_n(t) \phi_n(\vec{x}) \\ \ddot{\Gamma}_n(t) = -\alpha \dot{\Gamma}_n(t) - \omega_n^2 \Gamma_n(t) - \sum_{j=1}^{M_s} \rho_0 c_0^2 \phi_n^\perp(\vec{x}_{0j}) u_s^{\Omega_j}(\vec{x}_{0j}, t) \\ \quad + \sum_{j=1}^{M_s} \rho_0 c_0^2 \nabla_s \phi_n^\perp(\vec{x}_{0j}) \varphi^{\Omega_j}(\vec{x}_{0j}, t) + (\gamma - 1) \mathcal{H}_{i,n}^\perp Q(t) \end{cases} \quad (12)$$

which is an extension of Eq. (7) when the expansion is performed on the over-complete frame $(\phi_n)_{n \geq 1}$ instead of the orthogonal basis $(\psi_n)_{n \geq 1}$. This dynamical system governs the temporal evolution of the pressure field in the domain Ω_i , under normal velocity forcing $u_s^{\Omega_j}(\vec{x}_{0j}, t)$ and acoustic potential forcing $\varphi^{\Omega_j}(\vec{x}_{0j}, t)$ imposed by adjacent subsystems, as well as the volume forcing $Q(t)$ due to the presence of active flames within Ω_i . In the case of the orthogonal modal basis $(\psi_n)_{n \geq 1}$ used in the previous section, the terms $\nabla_s \psi_n^\perp(\vec{x}_{0j})$ vanish (since the eigenmodes satisfy rigid-wall boundary conditions on S_{ci}), and we have the simple relations $\psi_n^\perp(\vec{x}_{0j}) = \Delta S_{0j} \psi_n(\vec{x}_{0j})/\Lambda_n$ and $\mathcal{H}_{i,n}^\perp = \mathcal{H}_i^{(n)}/\Lambda_n$.

Because of the use of the over-complete frame $(\phi_n)_{n \geq 1}$, the acoustic pressure and velocity are free to evolve independently on the boundary S_{ci} , which is the major improvement of the method compared to classical formalism where the normal acoustic velocity $\vec{u} \cdot \vec{n}_s$ is necessarily zero on the connection boundary S_{ci} .

The governing dynamical system of Eq. (12) is a projection of the wave equation (Eq. (2)) onto the modal frame $(\phi_n)_{n \geq 0}$. However, as this frame is over-complete such projection is ill-conditioned, which constitutes one of the major pitfalls of the proposed method. The first consequence is a numerical difficulty to compute the inverse of the frame Gram matrix $\underline{\underline{\Delta}}^{-1}$. In most cases presented in this paper, the condition number $\overline{\underline{\underline{\Delta}}} = \|\underline{\underline{\Delta}}\| \|\underline{\underline{\Delta}}^{-1}\|$ increases with the size N of the expansion, up to values ranging from 10^{18} to 10^{19} . The inversion of this poorly conditioned matrix is achieved thanks to the use of an adequate numerical algorithm, based on extra-precision iterative refinement performed in floating-point quadruple precision. Errors stemming from this inversion are systematically computed *a posteriori* and verified to remain low. Note that since the modal basis size remains in practice limited (typically a few dozens elements), the specific inversion procedure used to calculate $\underline{\underline{\Delta}}^{-1}$ does not noticeably increase the computational cost in comparison to the classical rigid-wall modal expansion. Secondly, even though $\underline{\underline{\Delta}}$ is accurately inverted, the frame over-completeness may still result in poorly conditioned spurious components in Eq. (12). However, the approach described above produces well-behaved expansions for the pressure, that is expansions where the terms with the highest energy are physically meaningful while low energy terms represent spurious fluctuations. Thus, an energetic criterion for the robust and automatic identification of these spurious components was designed, as discussed in more details in Appendix C.

3. State-space formalism for subsystems coupling

The dynamical system derived in Section 2.2 allows us to solve for the acoustic pressure in each individual subdomain Ω_i . In order to resolve the acoustic flow in the whole geometry, individual subdomains need to be connected together. An elegant formulation to connect subdomains is to use a state-space approach. This method, already used in [32–34,41], is adopted in this work but requires to be adapted. Some implementation details are given below; further developments relative to state-space representations can be found in control theory textbooks [46].

For any physical system described by a set of coordinates $\underline{X}(t)$ in a phase-space, we call linear state-space representation of this system a set of equations under the form:

$$\begin{cases} \dot{\underline{X}}(t) = \underline{A} \underline{X}(t) + \underline{B} \underline{U}(t) \\ \underline{Y}(t) = \underline{C} \underline{X}(t) + \underline{D} \underline{U}(t) \end{cases} \quad (13)$$

where $\underline{X}(t)$ is the coordinates vector in the phase-space, also called state vector, \underline{A} is the dynamics matrix, \underline{B} is the input matrix, $\underline{U}(t)$ the input vector, $\underline{Y}(t)$ the output vector, \underline{C} the output matrix, and \underline{D} is the action, or feedthrough matrix. The first equation of the state-space representation governs the dynamical evolution of the state vector under the forcing exerted by the input vector. The second equation defines a way to compute any desired outputs from the knowledge of the state vector and the forcing term. Note that the output $\underline{Y}(t)$ depends on the state $\underline{X}(t)$, but the reverse is not true: $\underline{X}(t)$ evolves independently of the selected output $\underline{Y}(t)$. The state-space formalism, through the Redheffer star-product [47] (Supplemental Material C), provides a direct way to connect two systems represented by their state-space realizations, by relating their respective inputs and outputs. A simple example of this operation is given in Section 4.

By considering the dynamical system of Eq. (12), it is straightforward to build a state-space representation for a subdomain Ω_i . A convenient choice is to build the state-vector $\underline{X}^{(i)}(t)$ from the modal amplitudes $\tilde{\Gamma}_n(t)$ and their temporal primitives $\Gamma_n(t)$. The input vector $\underline{U}^{(i)}(t)$ contains the normal acoustic velocities $u_s^{\Omega_j}(\bar{x}_{0j}, t)$ and the acoustic potentials $\varphi^{\Omega_j}(\bar{x}_{0j}, t)$ imposed by adjacent subdomains Ω_j . The heat release volume source $Q(t)$ is also included in the input vector. Beside, the computed output vector $\underline{Y}^{(i)}(t)$ consists of the pressures $p(\bar{x}_{0j}, t)$ and the normal acoustic velocities $u_s(\bar{x}_{0j}, t)$ at every point \bar{x}_{0j} on the connection boundary S_{ci} . In addition, any quantity of interest that can be computed from the modal amplitudes contained in the state-vector $\underline{X}^{(i)}(t)$ may also be added in the output vector $\underline{Y}^{(i)}(t)$. For conciseness, the detailed expressions of the state-space matrices for a subdomain Ω_i are not given here, but can be found in Appendix A.

After iteratively applying the Redheffer star-product to connect together state-space representations of every subsystems, the full state-space of the whole geometry is obtained as:

$$\dot{\underline{X}}^f(t) = \underline{A}^f \underline{X}^f(t) + \underline{B}^f \underline{U}^f(t) \quad (14)$$

where $\underline{U}^f(t)$ is an external forcing that can be either a surface or a volume source term. In the former case, coefficients in the external input matrix \underline{B}^f contains terms similar to the first $2M_S$ columns $\underline{B}^{(i)}$ in Eq. (A.1), while in the latter case it contains terms similar to the last column of $\underline{B}^{(i)}$ in Eq. (A.1). Two approaches are then possible: (1) Eq. (14) can be integrated over time to obtain the temporal evolution of the acoustic flow under the external forcing $\underline{U}^f(t)$, or (2) the complex eigenvalues and eigenvectors of the dynamics matrix \underline{A}^f can be solved for, yielding the global acoustic eigenfrequencies and eigenmodes of the whole domain. If $\lambda_n = 2\pi\sigma_n + j2\pi f_n$ is the n^{th} complex eigenvalue of the matrix \underline{A}^f , then f_n is the eigenfrequency of the n^{th} acoustic mode of the whole geometry. In the absence of acoustic losses, volume sources or complex boundary impedances, σ_n is zero. Conversely, if the system comprises acoustic sources, then $2\pi\sigma_n$, is the growth-rate of the n^{th} acoustic mode of the whole geometry: $\sigma_n > 0$ (resp. $\sigma_n < 0$) implies that the mode is unstable (resp. stable). The mode shape can also be reconstructed from the modal components contained in the eigenvector \underline{v}_n associated to the eigenvalue λ_n .

4. Convergence properties

In this section both modal expansions presented in Section 2 are implemented within the LOM state-space framework introduced in Section 3, and used to study a canonical case, namely a long quasi-one-dimensional tube comprising a sharp cross-section change. The goal is to show the limits of the rigid-wall modes decomposition and to prove the performances of the over-complete frame approach in a case where both types of modal expansions can be evaluated and compared to an analytical

solution. In the following, superscripts ^{OB}(resp. ^{FR}) refer to results obtained with the use of the orthogonal basis $(\psi_n)_{n \geq 1}$ introduced in Section 2.1 (resp. the over-complete frame $(\phi_n)_{n \geq 1}$ introduced in Section 2.2). Superscripts ^A designate analytical solutions used for comparison.

In this example, the long duct with a sudden cross-section change represented in Fig. 2 is considered. Both ends of the duct are closed by rigid walls. It is decomposed into 3 subsystems, including 2 long ducts (Ω_1 and Ω_2) with constant cross-sections S_1 and S_2 , and a third subsystem Ω_{sc} of length L_{sc} enclosing the region in the neighborhood of the cross-section variation.

Since both tubes Ω_1 and Ω_2 are long ($D_1 \ll L_1$, $D_2 \ll L_2$), only plane longitudinal acoustic waves are considered here. The rigid-wall orthogonal bases of both ducts are then:

$$\begin{cases} (\psi_n^{(1)}(x_1))_{n \leq N_1} = \left(\cos\left(\frac{n\pi x_1}{L_1}\right) \right)_{n \leq N_1} \\ (\psi_n^{(2)}(x_2))_{n \leq N_2} = \left(\cos\left(\frac{n\pi x_2}{L_2}\right) \right)_{n \leq N_2} \end{cases} \quad (15)$$

where superscript ⁽¹⁾(resp. ⁽²⁾) refers to the modal basis in Ω_1 (resp. Ω_2), x_1 and x_2 are the longitudinal coordinates in the two ducts (Fig. 2), and N_1 (resp. N_2) is the number of modes used for the pressure modal expansion in Ω_1 (resp. Ω_2). Similarly the over-complete frames introduced in Section 2.2 for both ducts are given by:

$$\begin{cases} (\phi_n^{(1)}(x_1))_{n \leq N_1} = \left(\cos\left(\frac{n\pi x_1}{L_1}\right) \right)_{n \leq N_1/2} \\ \cup \left(\cos\left(\frac{(2n+1)\pi x_1}{2L_1}\right) \right)_{n \leq N_1/2} \\ (\phi_n^{(2)}(x_2))_{n \leq N_2} = \left(\cos\left(\frac{n\pi x_2}{L_2}\right) \right)_{n \leq N_2/2} \\ \cup \left(\sin\left(\frac{(2n+1)\pi x_2}{2L_2}\right) \right)_{n \leq N_2/2} \end{cases} \quad (16)$$

These orthogonal bases (Eq. (15)) and over-complete frames (Eq. (16)) are consistent with rigid-wall conditions at both end of the long duct ($x_1 = 0$ and $x_2 = L_2$). However, the orthogonal bases also impose zero velocity near the cross section change (at $x_1 = L_1$ and $x_2 = 0$), while the over-complete frames retain an additional degree of freedom such that both velocity and pressure are *a priori* undetermined and free to evolve independently near the cross-section change. In the following, the same number N of eigenmodes are used for modal expansions in both ducts ($N_1 = N_2 = N$). Additionally, all comparisons between orthogonal basis and over-complete frame expansions are carried out with the same total numbers of modes N : in other words results from any orthogonal basis containing an even number of vectors N are compared to results from a frame composed of two subfamilies of size $N/2$. Note also that, since only plane longitudinal waves are considered here, the connection boundaries S_{c1} and S_{c2} do not need to be discretized into several surface elements ΔS_{0j} : therefore $M_S = 1$ for each subdomain Ω_1 and Ω_2 , and $M_S = 2$ for Ω_{sc} .

Modal expansion is not performed for the subdomain Ω_{sc} enclosing the cross-section change as its exact geometry has only very little effect on the global eigenmodes of the long duct: instead, volume-averaged conservation equations are used to derive a state-space representation of this subsystem. More details are given in Appendix B. The Redheffer star-product (Supplemental Material C) is then applied recursively to connect state-space representations of subsystems Ω_1 , Ω_{sc} , and Ω_2 . The state-space real-

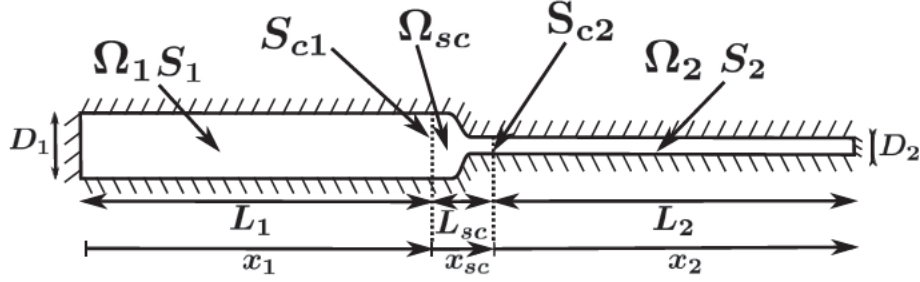


Fig. 2. A long duct comprising a sharp cross-section change. Hashed lines boundaries are rigid walls. The geometry is decomposed into 3 subsystems. Two of those are long ducts (Ω_1 and Ω_2), of respective lengths L_1 and L_2 , cross-sections S_1 and S_2 , and equivalent diameters D_1 and D_2 . The third subsystem Ω_{sc} is a small domain ($L_{sc} \ll L_1, L_2$) located around the cross-section change. S_{c1} and S_{c2} are connection surfaces between Ω_{sc} and the two tubes.

ization of the full geometry is then obtained as in Eq. (14):

$$\frac{d}{dt} \underbrace{\begin{pmatrix} \underline{X}^{(1)}(t) \\ \underline{X}^{(sc)}(t) \\ \underline{X}^{(2)}(t) \end{pmatrix}}_{\underline{X}^f(t)} = \underbrace{\begin{pmatrix} \underline{A}^{(1)} & \underline{B}^{(1)} \underline{C}^{(sc)} & 0 \\ \underline{B}_1^{(sc)} \underline{C}^{(1)} & \underline{A}^{(sc)} & \underline{B}_2^{(sc)} \underline{C}^{(2)} \\ 0 & \underline{B}^{(2)} \underline{C}^{(sc)} & \underline{A}^{(2)} \end{pmatrix}}_{\underline{A}^f} \begin{pmatrix} \underline{X}^{(1)}(t) \\ \underline{X}^{(sc)}(t) \\ \underline{X}^{(2)}(t) \end{pmatrix} \quad (17)$$

In this equation, matrices $\underline{A}^{(1)}$, $\underline{B}^{(1)}$, $\underline{C}^{(1)}$, $\underline{A}^{(2)}$, $\underline{B}^{(2)}$, and $\underline{C}^{(2)}$, are the state-space representations of subdomains Ω_1 and Ω_2 , as defined in Section 3 and Appendix A. Matrices $\underline{A}^{(sc)}$, $\underline{B}_1^{(sc)}$, $\underline{B}_2^{(sc)}$, $\underline{C}_1^{(sc)}$ and $\underline{C}_2^{(sc)}$ are used in the state-space representation of the subdomain Ω_{sc} and are given in Appendix B. The extra-diagonal blocks of the matrix \underline{A}^f represent coupling between the two ducts Ω_1 and Ω_2 and the subdomain Ω_{sc} enclosing the section change. In the present case, the matrices $\underline{A}^{(1)}$ and $\underline{A}^{(2)}$ share the same size $2N$ (see Eq. (A.1)), and from Eq. (B.1), $\underline{A}^{(sc)}$ is a 3×3 matrix. Thus, the dynamical system governing the pressure evolution in the whole geometry is of size $4N + 3$. The corresponding acoustic eigenfrequencies and eigenmodes are obtained by solving for the eigenvalues and eigenvectors of \underline{A}^f . Resulting eigenfrequencies are noted $f_n^{OB}(N)$ if the rigid-wall orthogonal basis is used, and $f_n^{FR}(N)$ if the pressure is expanded onto the over-complete frame of Section 2.2. The corresponding pressure mode shapes are $\Upsilon_{n,p}^{OB}(x; N)$ and $\Upsilon_{n,p}^{FR}(x; N)$, and finally the velocity mode shapes are $\Upsilon_{n,u}^{OB}(x; N)$ and $\Upsilon_{n,u}^{FR}(x; N)$.

In the following example the cross-section change is located at $1/3$ of the duct length ($L_1 = L_2/2 = L$), and the cross-section ratio is such that $S_1 = 2S_2$. Under the compactness assumption ($L_{sc} \ll L_1, L_2$) the analytical frequency reads:

$$f_n^A = \frac{nc_0}{2L} \text{ if } n = 0 \text{ modulo } 3, \\ \text{or } f_n^A = \frac{nc_0}{L} \pm \frac{c_0}{\pi L} \arctan((2 \pm \sqrt{3})^{1/2}) \text{ otherwise} \quad (18)$$

For the first mode ($n = 1$), the analytical pressure and velocity modal shapes write:

$$\Upsilon_{1,p}^A(x) = \begin{cases} -\frac{1}{\sqrt{3}} \cos\left(\frac{\lambda x_1}{L}\right), & \text{in } \Omega_1 \\ \cos\left(\frac{2\lambda(x_2 - 2L)}{2L}\right), & \text{in } \Omega_2 \end{cases} \quad (19)$$

$$\Upsilon_{1,u}^A(x) = \begin{cases} \frac{1}{\sqrt{3}\rho_0 c_0} \sin\left(\frac{\lambda x_1}{L}\right), & \text{in } \Omega_1 \\ -\frac{1}{\rho_0 c_0} \sin\left(\frac{2\lambda(x_2 - 2L)}{2L}\right), & \text{in } \Omega_2 \end{cases} \quad (20)$$

where $\lambda = 2 \arctan((2 - \sqrt{3})^{1/2})$. Note that for the first mode both pressure and velocity are non-zero at the cross-section change ($x_1 = L, x_2 = 0$).

In Fig. 3, the pressure and velocity mode shapes for the first mode ($n = 1$) are displayed and compared to the analytical solutions of Eqs. (19) and (20).

The use of the rigid-wall eigenmodes expansions defined in Eq. (15) provides numerical solutions for the pressure mode shape that converge towards the analytical solution when the number N of modes in the orthogonal basis increases (Fig. 3(a)–(c)). However, the closeup view on the region near the cross-section change (Fig. 3(d)–(f)) shows a slight discrepancy in the pressure modal shape. Fig. 3(g)–(i) support this observation by evidencing a strong singularity in the velocity mode shape, which results in an erroneous representation of the velocity mode over a large region of the domain. This singularity is the direct consequence of the use of the rigid-wall eigenmodes expansion: the numerical velocity $\Upsilon_{1,u}^{OB}(x)$ is indeed zero at the cross-section change (because the derivative of ψ_n in Eq. (15) is zero for $x_1 = L$ and $x_2 = 0$), in contradiction with the analytical solution $\Upsilon_{1,u}^A(x)$ at this point (see Eq. (20) for $x_1 = L$ or $x_2 = 0$). Most importantly, increasing the number N of modes in the modal basis fails to suppress this singularity, but rather results in higher frequency oscillations around the cross section area change. These spatial fluctuations suggest a Gibbs-like phenomenon affecting the convergence of the velocity representation, typical of Fourier series expansions of irregular functions. These oscillations on the velocity in the vicinity of the duct contraction may be critical in thermoacoustics, since the velocity is the input of the classical Flame Transfer Function used to model flame-acoustic coupling.

On the contrary, as shown in Fig. 4, modal expansions onto the over-complete frames of Eq. (16) accurately represent the analytical solutions $\Upsilon_{1,p}^A(x)$ and $\Upsilon_{1,u}^A(x)$, even for a number of modes as low as $N = 4$, as the local absolute error does not exceed 3×10^{-4} for the pressure, and 5×10^{-6} for the velocity.

The relative error for the n^{th} global eigenfrequency is defined as (with similar definition for FR):

$$E_{f_n}^{OB}(N) = \frac{|f_n^A - f_n^{OB}(N)|}{f_n^A} \quad (21)$$

Figure 5 provides the convergence behavior for the global eigenfrequencies of modes 1, 9, and 11. It appears that the method based on orthogonal bases expansions present a relatively slow convergence speed for eigenfrequencies f_1 and f_{11} . This poor convergence is due to the Gibbs phenomenon affecting the numerical solution for the velocity mode $\Upsilon_{1,u}^{OB}(x)$ in the vicinity of the cross-section change. Mode 9 however, is accurately resolved even for small values of N ; this is because it naturally has a velocity node at the cross-section change (Eq. (20)) and is therefore, by chance, not subjected to the Gibbs phenomenon. In contrast, the method relying on modal expansions onto over-complete frames

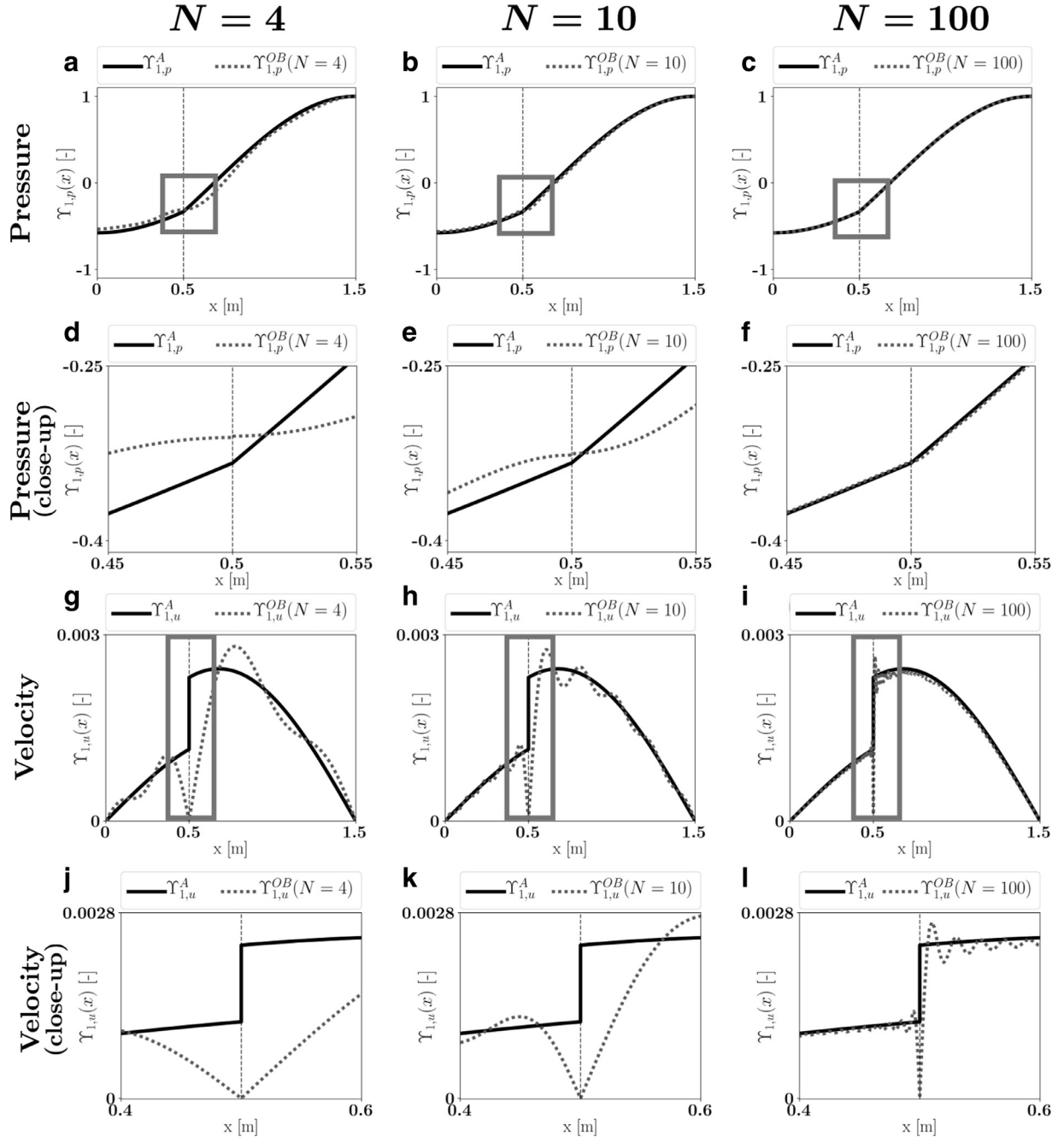


Fig. 3. Pressure mode shape and velocity mode shape of the first mode ($n = 1$), for $N = 4, 10, 100$ vectors in the OB expansion. Computed solutions (gray dashed lines) are compared to the analytical solutions of Eqs. (19) and (20) (thick dark lines). Closeup views (corresponding to the rectangles) of the pressure and the velocity mode shapes are given on the second row ((d)–(f)) and the fourth row ((j)–(l)) respectively.

results in low relative errors, ranging between 10^{-7} and 10^{-8} for all modes 1, 9 and 11, even with small values of N . For instance, only about 10 modes in each frame are necessary to accurately capture the eigenfrequency f_{11} . The condition number of the frame Gram matrix, which is an indicator of the expansion over-completeness, is $C(\underline{\Lambda}) = 10^8$ for $N = 6$. It then progressively deteriorates and reaches 10^{19} at $N = 50$, and saturates to this value for large N . This deterioration of the frame conditioning does not result into a degradation of the numerical results. However, it can be related to a saturation of the error, since increasing the size of the frame beyond $N = 20$ does not result in smaller errors.

Finally, it is worth emphasizing that Gibbs fringes have also been reported in earlier studies employing orthogonal basis modal

expansions, for instance by Sayadi et al. [40]. However, the origin of these Gibbs oscillations was fundamentally different from those observed in the present example: in previous works, this phenomenon was caused by the presence of an infinitely thin region of fluctuating heat release located in the interior of the domain of interest. This assumption results in an *exact* solution for the velocity field that is *discontinuous* at the flame location, and that cannot be accurately represented by a classical Galerkin decomposition. The over-complete frame expansion presented in this work aims at suppressing Gibbs oscillations due to a misrepresentation of the acoustic fields at the boundaries of the subdomains, and does not have the ability to handle Gibbs fringes produced by a discontinuity in the interior of the subdomains. Nonetheless, a simple workaround to handle this latter case is to replace the in-

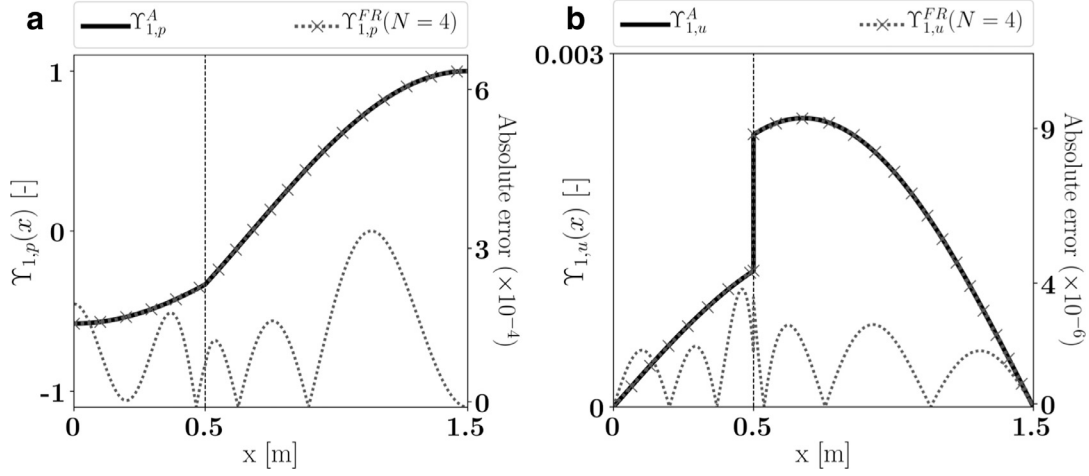


Fig. 4. Pressure mode shape (a) and velocity mode shape (b) of the first mode ($n = 1$) for $N = 4$ vectors in the frame. Numerical solutions (gray lines with \times) are compared to the analytical solutions of Eqs. (19) and (20) (thick dark lines). The local absolute errors for the mode shapes with $N = 4$ are also plotted (dashed line), with values indicated on the right axis.

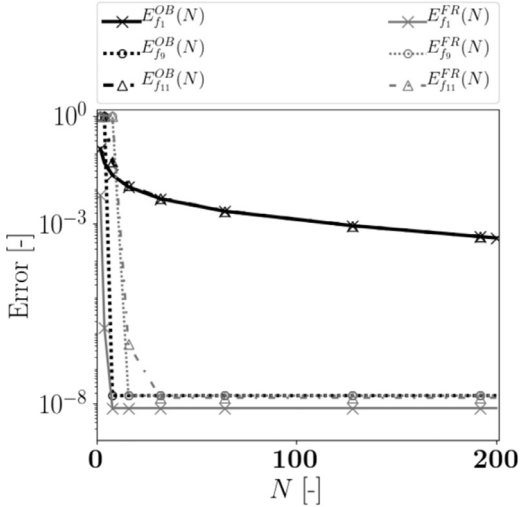


Fig. 5. Comparison between the OB and the FR results in terms of frequency relative error ($E_{f_n}^{OB/FR}$), for global modes 1, 9 and 11, in function of the number N of vectors used in the modal expansions. Dark lines are results obtained with rigid-wall eigenmodes expansions (Eq. (15)), while gray lines are results obtained with frames modal expansions (Eq. (16)).

finitely thin flame by a slightly thicker region of heat release: this yields a solution for the velocity field that has a sharp yet continuous spatial variation in the vicinity of the flame. Note also that infinitely thin flame are interesting conceptually and from an analytical perspective; however, physical flames are always finite and sometimes thick enough to produce non-compact effects on thermoacoustic instabilities [48].

5. Application to thermoacoustic instabilities in an annular combustor

In order to demonstrate its ability to predict thermoacoustic instabilities in complex geometries, the state-space LOM based on generalized frame modal expansions (FR) is now applied to a more advanced academic configuration comprising active flames in an annular chamber. Results obtained with the classical orthogonal rigid-wall basis (OB) are also provided and compared to those computed with a 3D Finite Element (FE) solver called AVSP [5]. The geometry studied is displayed in Fig. 6(a), and the correspond-

ing low-order acoustic network is represented in Fig. 6(b). It comprises an annular plenum (denoted with the subscript p), an annular chamber (subscript c), and four identical ducted burners (subscript B) of length L_B where the active flames are located. Rigid-wall boundary conditions are assumed at the plenum back-plane and the chamber outlet plane.

The AVSP unstructured mesh consists of 3×10^6 tetrahedral cells, while the acoustic network contains 14 subdomains (1 plenum Ω_p , 1 chamber Ω_c , 4 burners Ω_{B_i} , and 8 cross-section changes Ω_{sc_i}), with the addition of 4 active flames. The flames H_i are located at the coordinate αL_B within each burner, and are considered as planar volume source of thickness δ . Note that the cross-section area S_B of the ducted burners is much smaller than the area of the plenum exit plane and of the chamber back-plane. This allows for the simplification of the plenum-burner and burner-chamber junctions, by only considering discrete point-like connections. In other words, the chamber (or the plenum) is connected to the burner Ω_{B_i} through the subdomain Ω_{sc_i} at a single point, implying that $M_S = 4$ for the chamber and the plenum (a single discrete connection surface $\Delta S_{O_j} = S_B$ is used for each one of the 4 burners). The subdomain Ω_{sc_i} is similar to the cross-section change described in the previous section, as it essentially enforces continuity of pressure and acoustic flux between the burner end and the backplane of the chamber (or the exit plane of the plenum). This simplification also allows us to consider rigid-wall boundary conditions at the chamber backplane and at the plenum exit plane when defining the eigenmodes for these subdomains (since the velocity should actually be non-zero only at 4 point-like locations of infinitely small spatial extent). The Gibbs phenomenon evidenced in the previous section is then not expected to appear in the chamber and in the plenum, and it is therefore valid to employ orthogonal rigid-wall bases in these two subdomains. On the contrary, boundary conditions at both ends of the burners are expected to differ from rigid-wall or open atmosphere, and it is therefore necessary to employ over-complete frame expansions in these subdomains in order to mitigate the Gibbs phenomenon that may appear. Thus, the plenum is modeled as a 2D annular subdomain of coordinates (x_p, θ_p) , whose orthogonal basis is:

$$\psi_{n,m}^{(p)}(x_p, \theta_p) = \left(\cos\left(\frac{n\pi x_p}{L_p}\right) \cos(m\theta_p), \cos\left(\frac{n\pi x_p}{L_p}\right) \sin(m\theta_p) \right) \quad (22)$$

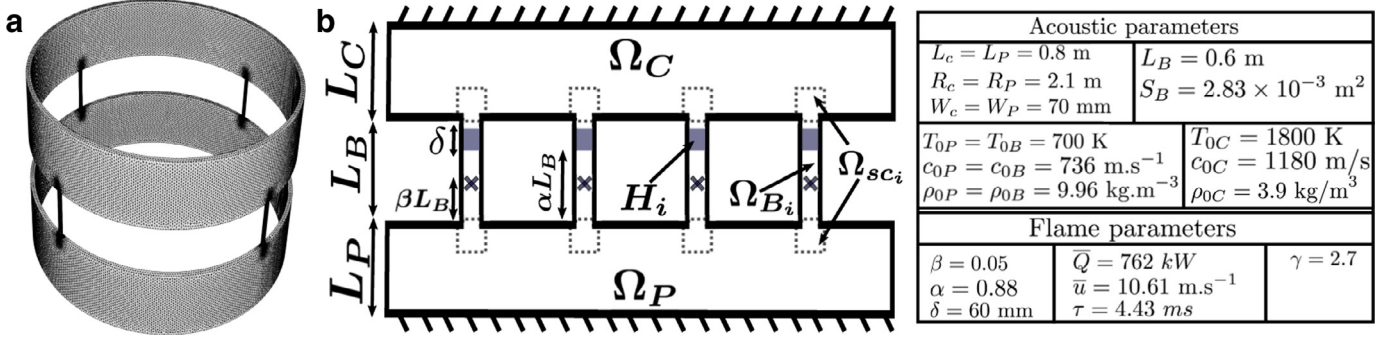


Fig. 6. (a) The unstructured mesh used in the AVSP FE solver. (b) The low-order thermoacoustic network representing this system, which consists of an annular plenum Ω_P , 4 burners Ω_{B_i} , an annular chamber Ω_C , and a set of 8 subdomains Ω_{sc_i} containing the cross-section changes. Thick dark lines represent rigid-wall boundary conditions. Gray area (H_i) are the active flames, and the crosses represent the reference points used in the definition of the flame response. The width of the plenum (resp. chamber) in the radial direction is W_P (resp. W_C). All required numerical values for acoustic and flame parameters are indicated in the table.

Pressure in the chamber could be expanded onto an analogous analytical modal basis. However, this one is deliberately assumed analytically unknown, and a modal basis computed thanks to a preliminary AVSP simulation of the isolated chamber (without the burners and the plenum) is used instead. Note that it is not necessary to perform an AVSP simulation for each LOM simulation: it is indeed preferable to generate the chamber modal basis and all related quantities (including the matrix $\underline{\Delta}^{-1}$) in a single preliminary AVSP simulation, and to assemble the state-space realization of this subdomain, which can then be employed in as many LOM simulations as desired. In the present example, the use of a numerically computed modal basis demonstrates the ability of the present framework to combine in an acoustic network subdomains of different types and thus to handle efficiently arbitrarily complex systems.

In the following, the size of the modal bases in the chamber and in the plenum is fixed to $N = 12$ modes. For cases where the rigid-wall basis is used in the ducted burners, this one is the same as in the previous section (Eq. (15)). If an over-complete frame is used, it is given by:

$$(\phi_n^{(B)}(x_B))_{n \leq N} = \left(\cos\left(\frac{n\pi x_B}{L_B}\right) \right)_{n \leq N/2} \cup \left(\sin\left(\frac{n\pi x_B}{L_B}\right) \right)_{n \leq N/2} \quad (23)$$

Note the difference with the over-complete frame of Eq. (16), as the present one allows pressure and velocity to evolve independently from one another at *both ends* of the duct.

Active flames are located within each burner, and the flame shape $\mathcal{H}_i(x_B)$ is the rectangular function of thickness δ centered around $x_B = \alpha L_B$. The flame response is modeled thanks to a classical Flame Transfer Function (FTF), relating the fluctuations of heat release to the fluctuations of acoustic velocity at a reference point located at $x_B^{(ref)} = \beta L_B$. The flame reference point is located in the burners, near the plenum exit-plane ($\beta = 0.05$). A simple constant-delay FTF is assumed, such that in the frequency domain the fluctuating heat release rate reads:

$$\hat{Q}(\omega) = \bar{Q} e^{-j\omega\tau} \left(\frac{\hat{u}(x_B = \beta L_B, \omega)}{\bar{u}} \right) \quad (24)$$

where \bar{Q} is the flame power, τ is the flame delay, and \bar{u} is the mean flow speed through the injector. A state-space realization of the time-delay $e^{-j\omega\tau}$ is generated thanks to a Multi-Pole expansion:

$$e^{-j\omega\tau} \approx \sum_{k=1}^{M_{PBF}} \frac{-2a_k j\omega}{\omega^2 + 2c_k j\omega - \omega_{0k}^2} \quad (25)$$

where each term in the sum is called a Pole Base Function (PBF). The coefficients a_k, c_k, ω_{0k} are determined thanks to a recursive fitting algorithm recently proposed by Douasbin et al. [49]. By making use of the inverse Fourier transform, it is then straightforward to convert this frequency domain transfer function into a time-domain state-space realization of size $2M_{PBF} \times 2M_{PBF}$, whose expression is provided in Appendix D. This procedure to generate a state-space realization of a FTF was already used by Ghirardo et al. [50]. For the flame-delay considered here, 12 PBFs were observed to be sufficient to accurately fit the term $e^{-j\omega\tau}$, yielding 24 DoF for each flame in the state-space representation of the whole system. Finally, the 18 state-space representations of the 14 acoustic subdomains and 4 active flames are connected together.

As mentioned earlier, the Gibbs phenomenon is expected to occur at both ends of the ducted burners. A particular attention is therefore paid to the type of modal expansion carried out in these subdomains. A total of 4 LOM simulations are performed, and results are compared to the ones computed with the FE solver AVSP, which are used as reference. Results for 10 of the first modes of the combustor are summarized in Table 1. First of all, FR and OB expansions with $N = 10$ modes are both compared to AVSP. Then these computations are repeated with a number of modes increased to $N = 30$. Mode 1 is the combustor Helmholtz mode, and its frequency and growth rate were observed to be very sensitive to the addition of a correction length to the ducted burners. As the determination of the optimal correction length is out of the scope of this paper, differences regarding the Helmholtz mode are not further discussed. The FR expansion with $N = 10$ appears to successfully resolve the frequencies and growth rates of the modes considered, with relative errors compared to AVSP below 10%. On the contrary, the OB expansion onto $N = 10$ modes largely fails at resolving the growth rates of all but one of the considered modes, with relative errors up to 348% (Mode 5). Mode 3 is the first unstable azimuthal mode of the combustor, and is therefore of particular interest: FR expansion yields an error of only 6% for the growth rate of this mode, whereas OB expansion produces an error of 45%. When the size of the expansion basis/frame is increased, results are globally improved for both FR and OB cases. Yet, even with $N = 30$ the OB approach still fails at achieving an acceptable accuracy for Modes 3, 5, and 7. The error on the growth rate of the first unstable azimuthal mode is of 0.3% in the FR case, while it is still overestimated by 18% in the OB case. Modes 9 and 10 are mixed modes, similar to those described by Evesque and Polifke[37]. In mode 9 the plenum first longitudinal mode prevails, while mode 10 is the mixed 1st-azimuthal-1st-longitudinal plenum mode, coupled with the 5th azimuthal chamber mode. Previous comments also applies to these mixed modes: the over-complete frame ex-

Table 1

Frequencies (f) and growth rates (σ) for 10 of the first thermoacoustic eigenmodes of the annular combustor considered. FE (AVSP) results serve as reference. Low-order simulations are performed with FR/OB expansions, first onto $N = 10$ modes, and then onto $N = 30$ modes. Gray cells indicate frequencies/growth rates for which the relative error in comparison to AVSP is greater than 10%. The corresponding values of the relative errors are written between parentheses.

Mode	FE (AVSP)		FR ($N = 10$)		OB ($N = 10$)		FR ($N = 30$)		OB ($N = 30$)	
	f (Hz)	σ (s^{-1})	f (Hz)	σ (s^{-1})	f (Hz)	σ (s^{-1})	f (Hz)	σ (s^{-1})	f (Hz)	σ (s^{-1})
1	37.5	6.05	38.0	6.37	37.0	10.4 (72%)	38.0	7.0 (16%)	40.3	7.7 (27%)
2	56.5	-1.08	56.4	-1.11	57.3	-1.9 (76%)	56.5	-1.1	56.4	-1.07
3	91.9	14.25	91.7	15.1	86.1	7.9 (46%)	90.6	14.3	91.5	16.8 (18%)
4	111.6	0.0	111.6	0.0	111.6	0.0	111.6	0.0	111.6	0.0
5	116.9	13.7	117.0	13.9	115.6	-34.0 (348%)	117.5	12.7	116.3	15.1 (10%)
6	167.6	0.37	167.6	0.37	167.3	0.47 (27%)	167.6	0.37	167.6	0.35
7	271.2	1.44	271.4	1.5	270.7	2.95 (105%)	271.4	1.5	271.8	1.8 (25%)
8	328.4	27.9	330.2	27.4	333.0	0.09 (100%)	330.0	26.8	329.5	29.8
9	454.9	0.02	454.8	0.02	454.7	0.04 (100%)	454.9	0.02	454.9	0.03 (50%)
10	458.3	0.06	458.2	0.065	458.0	0.09 (50%)	458.2	0.065	458.2	0.064

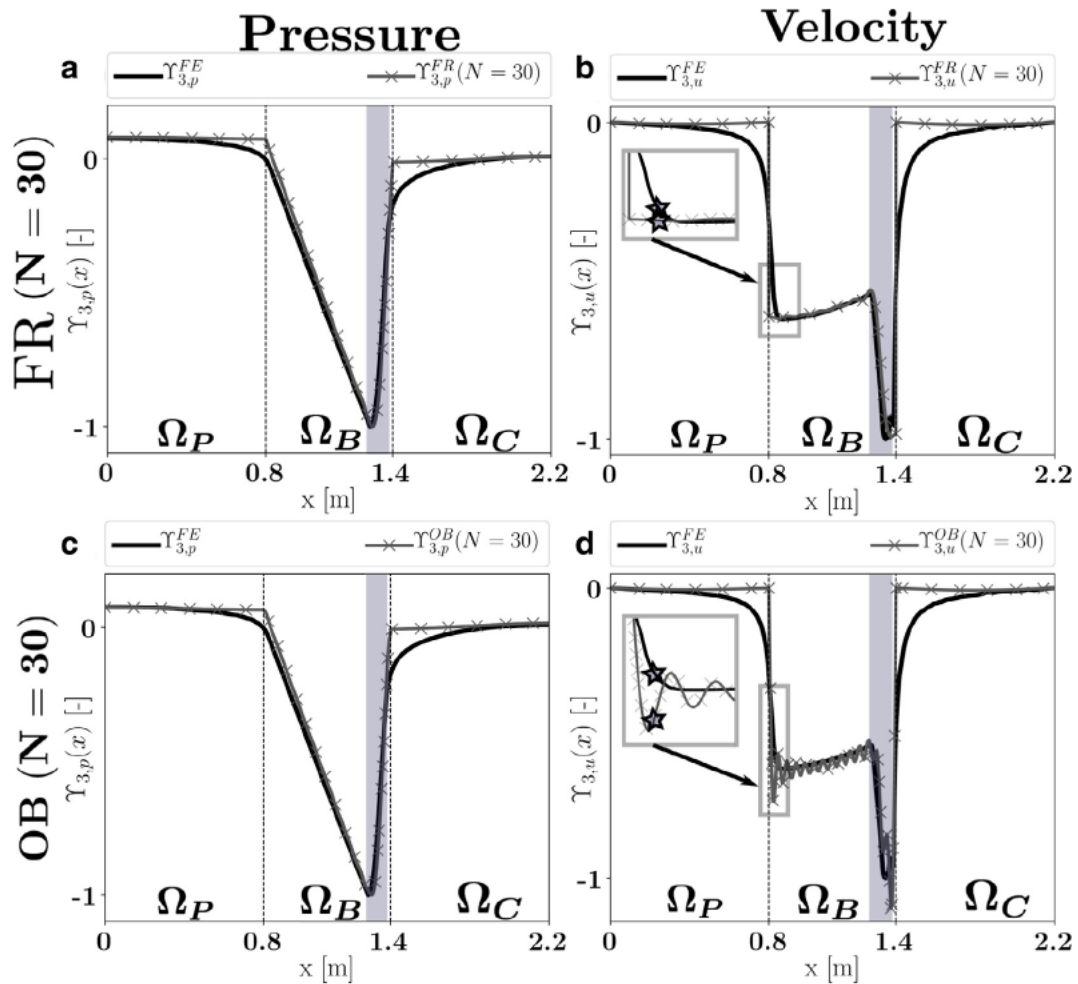


Fig. 7. Pressure and velocity mode shapes for Mode 3, plotted over a line extending from the bottom of the plenum to the end of the chamber and passing through a burner. Thick dark lines are results of AVSP computations. Gray lines with crosses are results of the LOM computations with $N = 30$ modes. Vertical dashed lines are the separation between the subdomains in the LOM network. Gray area represent the location of the active flames. First column: (a) pressure mode shape in the FR case; (c) pressure mode shape in the OB case. Second column: (b) velocity mode shape in the FR case, with a closeup view around the location of the flame reference point, which is represented by a star; (d) velocity mode shape in the OB case, with the same closeup view.

pansion of size $N = 10$ yields an excellent agreement with the FE solver, and outperforms even larger orthogonal basis expansions. Note that in the FR case, the condition number of the frame Gram matrix used in the 4 ducted burners is of order 10^8 for $N = 10$, and increases to 10^{18} for $N = 30$. It was verified that increasing the frame size does not further deteriorates its conditioning: it instead saturates at 10^{18} even for large N .

The relatively poor accuracy of the OB expansion LOM is explained by a closer examination of the modes shapes in the burners. Figure 7 shows the shape of the first unstable azimuthal mode of the combustor (Mode 3), plotted over a line starting from the bottom of the plenum, passing through a burner, and ending at the chamber outlet plane. With $N = 30$, both FR and OB pressure mode shapes (Fig. 7(a) and (c)) are relatively close to the AVSP computation, except for 3D effects in the neighborhood of the subdomains connections that cannot be captured. On the contrary, Fig. 7(d) shows that the OB expansion produces significant Gibbs oscillations of the velocity at both ends of the burner. Note that the Gibbs phenomenon is only present at the ends of the burners, and does not affect the velocity field within the chamber and the plenum. Conversely, Fig. 7(b) shows that the frame expansion successfully mitigates this Gibbs phenomenon.

The conjugation of these spurious oscillations with the presence of active flames responding to velocity fluctuations explains the large discrepancies observed in the growth rates. Indeed, the closeup view displayed in Fig. 7(d) reveals that the flame reference point (represented by a star) lies in a region where the velocity is strongly affected by Gibbs oscillations. In contrast, the FR expansion (Fig. 7(b)) yields a reference velocity close to the AVSP reference velocity. As heat release fluctuations are directly proportional to the reference velocity (Eq. (24)), any misprediction of the velocity in the burner results in a potentially erroneous growth rate. Thus, should the point of reference lies in a region where numerical oscillations are present, the computed thermoacoustic modes may strongly depend on unphysical and uncontrolled details such as the relative position of the point of reference and the Gibbs oscillations. Consequently, the orthogonal rigid-wall basis expansion results in a LOM that is highly sensitive to the location of the flame reference point, which is a highly undesirable feature of a numerical model.

This example demonstrates the modularity of the proposed LOM, which can combine in a same thermoacoustic network active flames, one-dimensional subdomains (the burners), 2D subdomains (the plenum), and complex 3D subdomains of arbitrary shape (the chamber) for which the modal basis is numerically computed. Obviously, the approach is not limited to azimuthal eigenmodes, but is also able to capture any other form of thermoacoustic eigenmodes. It is also worth comparing the cost associated to the over-complete frame expansion LOM to existing Low-Order Models. As shown above, $N = 10$ modes were sufficient to achieve a satisfactory resolution (with error below 10%) of the first 20 modes of the combustors (not all shown in Table 1). The state-space of the whole system comprises 248 DoF: 2×24 for the plenum and the chamber, 4×20 for the straight ducts, 8×3 for the cross-section changes, and 4×24 for the active flames. After the preliminary computation of the chamber modal basis with AVSP (160 CPU seconds for 12 modes), the LOM computation of all the eigenmodes was performed in a few CPU seconds only. This is comparable to the 300 DoF necessary to treat a similar annular configuration in the work of Schuermans and co-workers [33,35]. However, unlike this latter method, the present example did not assume acoustically compact injectors represented as lumped elements, and the acoustic field is fully resolved within the burners. LOMs relying on direct discretization of the flow domain, although more straightforward to put into application, appears to result in more DoF and higher cost: Emmert et al. [41] required 10^5 DoF and 38 CPUs to

compute 5 eigenmodes of a 12-injectors annular geometry without any active flames. Finally, in contrast to mixed-method LOMs based on modal expansions alongside Riemann invariants A^+/A^- [14], the proposed Low-Order Model (Eq. (14)) can be directly integrated in time for temporal simulations of thermoacoustic instabilities, whereas the time-domain translation of Riemann invariants appears to be somehow constraining [51].

6. Conclusions

This work addressed a known issue in LOMs for thermoacoustics, namely the misrepresentation of the acoustic field arising from modal expansions onto rigid-wall eigenmodes bases, already reported by numerous earlier studies [24]. Under the assumption of zero Mach number flow, a reformulation of the classical modal expansion making use of over-complete frames of eigenmodes was proposed for the first time. Two major observations were drawn from the analysis of a simple one-dimensional acoustic problem: (1) the modal expansion singularity was clearly identified as a Gibbs-like phenomenon affecting the acoustic velocity, resulting in slow convergence speeds and erroneous velocity values near junctions between subdomains; (2) the over-complete frame expansion was shown to successfully suppress the Gibbs-like phenomenon and to yield significantly improved convergence speeds. The only pitfall stemming from the frame expansion, lies in its over-completeness that may entail ill-conditioned features, which may produce spurious, non-physical dynamics of the pressure evolution. Thus, a specific inversion procedure is used to compute \underline{A}^{-1} , the inverse of the frame Gram matrix. This approach ensures that these spurious components stay negligible in comparison to physically meaningful components. More rigorously, in Appendix C it is demonstrated that spurious eigenmodes arising from the frame over-completeness have low energy, and a criterion is derived to systematically identify them.

In a second example, the generalized modal expansion LOM was used to predict thermoacoustic instabilities in an annular combustor. It was shown to yield results close to a finite element solver, whereas the rigid-wall modal expansions failed at accurately predicting the linear growth rates. This second example also demonstrates the modularity of the proposed framework, through its ability to combine in a same acoustic network highly heterogeneous classes of elements such as active flames, one-dimensional ducts, or complex 3D cavities. From a practical point of view, the implementation of the proposed method only requires minimal changes to existing algorithms based on rigid-wall expansions. Namely, apart from the inversion of the Gram matrix and the identification of spurious eigenmodes, the input/output relations of each subdomain composing the acoustic network should be adapted to include both pressure and velocity at the boundaries. Thus, this novel method is expected to be potentially useful in the field of thermoacoustics.

Acknowledgments

The first author would like to thank the French Ministry of Higher Education, Research and Innovation and the Ecole Normale Supérieure de Paris-Saclay for funding this work through the CDSN scheme.

Appendix A. State-space realization of an acoustic subdomain

The state-space representation for a subdomain Ω_i belonging to an acoustic network is given in this section. The dynamical system of Eq. (12) governing the evolution of the acoustic pressure in the

subdomain Ω_i yields the following state-space realization:

$$\begin{aligned}
\frac{d}{dt} \underbrace{\begin{pmatrix} \Gamma_1(t) \\ \Gamma_1(t) \\ \vdots \\ \Gamma_N(t) \\ \Gamma_N(t) \end{pmatrix}}_{\underline{X}^{(i)}(t)} &= \underbrace{\begin{pmatrix} 0 & 1 & & & & \\ -\omega_1^2 & -\alpha & & & & \\ & & \ddots & & & \\ & & & 0 & 1 & \\ & & & -\omega_N^2 & -\alpha & \end{pmatrix}}_{\underline{A}^{(i)}} \underbrace{\begin{pmatrix} \Gamma_1(t) \\ \Gamma_1(t) \\ \vdots \\ \Gamma_N(t) \\ \Gamma_N(t) \end{pmatrix}}_{\underline{X}^{(i)}(t)} \\
+ \rho_0 c_0^2 \underbrace{\begin{pmatrix} 0 & 0 & \dots & 0 & 0 & 0 \\ -\phi_1^+(\bar{x}_1) & \nabla_s \phi_1^+(\bar{x}_1) & \dots & -\phi_1^+(\bar{x}_{M_S}) & \nabla_s \phi_1^+(\bar{x}_{M_S}) & \frac{\gamma-1}{\rho_0 c_0^2} \mathcal{H}_{i,1}^+ \\ \vdots & \vdots & \ddots & \vdots & \vdots & \vdots \\ 0 & 0 & \dots & 0 & 0 & 0 \\ -\phi_N^+(\bar{x}_1) & \nabla_s \phi_N^+(\bar{x}_1) & \dots & -\phi_N^+(\bar{x}_{M_S}) & \nabla_s \phi_N^+(\bar{x}_{M_S}) & \frac{\gamma-1}{\rho_0 c_0^2} \mathcal{H}_{i,N}^+ \end{pmatrix}}_{\underline{B}^{(i)}} \underbrace{\begin{pmatrix} \Gamma_1(t) \\ \Gamma_1(t) \\ \vdots \\ \Gamma_N(t) \\ \Gamma_N(t) \end{pmatrix}}_{\underline{X}^{(i)}(t)} \\
\times \underbrace{\begin{pmatrix} u_s^{\Omega_1}(\bar{x}_1, t) \\ \varphi^{\Omega_1}(\bar{x}_1, t) \\ \vdots \\ u_s^{\Omega_{M_S}}(\bar{x}_{M_S}, t) \\ \varphi^{\Omega_{M_S}}(\bar{x}_{M_S}, t) \\ Q(t) \end{pmatrix}}_{\underline{U}^{(i)}(t)} \quad (A.1)
\end{aligned}$$

In this equation, the state vector $\underline{X}^{(i)}(t)$ is of size $2N$, where N is the number of eigenmodes used in the modal expansion. The dynamics matrix $\underline{A}^{(i)}$ is block-diagonal of size $2N \times 2N$. The first $2M_S$ columns of the input matrix $\underline{B}^{(i)}$ and $2M_S$ elements of the input vector $\underline{U}^{(i)}(t)$ correspond to surface source terms imposed by adjacent subdomains Ω_j . The last column of $\underline{B}^{(i)}$ and the last element of $\underline{U}^{(i)}(t)$ correspond to the volumetric heat release forcing. For clarity reason, a single source of heat release is considered here, but the input can easily be extended to any number of independent flames.

In the state-space framework that is presented here, any subsystem Ω_i outputs both the normal velocity $u_s(\bar{x}_{0j}) = \bar{u}(\bar{x}_{0j}) \cdot \bar{n}_s$ and the pressure $p(\bar{x}_{0j})$ at each one of the M_S connection surface elements ΔS_{0j} . In addition, it is also possible to incorporate in the output vector (not detailed here) pressure and velocity at any point within Ω_i , such that those can then be passed as reference pressure/velocity to an active flame. Thus, the following equation is used to compute the output vector for the subdomain Ω_i :

$$\begin{aligned}
\underbrace{\begin{pmatrix} u_s(\bar{x}_1, t) \\ p(\bar{x}_1, t) \\ \vdots \\ u_s(\bar{x}_{M_S}, t) \\ p(\bar{x}_{M_S}, t) \end{pmatrix}}_{\underline{Y}^{(i)}(t)} &= \underbrace{\begin{pmatrix} -\frac{1}{\rho_0} \nabla_s \phi_1(\bar{x}_1) & 0 & \dots & -\frac{1}{\rho_0} \nabla_s \phi_N(\bar{x}_1) & 0 \\ 0 & \phi_1(\bar{x}_1) & \dots & 0 & \phi_N(\bar{x}_1) \\ \vdots & \vdots & \ddots & \vdots & \vdots \\ -\frac{1}{\rho_0} \nabla_s \phi_1(\bar{x}_{M_S}) & 0 & \dots & -\frac{1}{\rho_0} \nabla_s \phi_N(\bar{x}_{M_S}) & 0 \\ 0 & \phi_1(\bar{x}_{M_S}) & \dots & 0 & \phi_N(\bar{x}_{M_S}) \end{pmatrix}}_{\underline{C}^{(i)}} \underbrace{\begin{pmatrix} \Gamma_1(t) \\ \Gamma_1(t) \\ \vdots \\ \Gamma_N(t) \\ \Gamma_N(t) \end{pmatrix}}_{\underline{X}^{(i)}(t)} \quad (A.2)
\end{aligned}$$

Note that the feedthrough matrix \underline{D} is zero. At the end, the state-space representation of the acoustics in the subdomain Ω_i is defined by Eqs. (A.1) and (A.2). It is a $2M_S$ -input $2M_S$ -output sys-

tem (in the absence of heat release source terms), whose dynamics are described by a $2N \times 2N$ matrix.

Appendix B. State-space representation for the domain Ω_{sc} enclosing the cross-section change

In this section, the state-space representation for the acoustically compact subdomain Ω_{sc} enclosing the cross-section change between the two ducts is given. It is obtained by volume-averaging the linearized Euler equations in Ω_{sc} , neglecting any acoustic conversion to the vortical mode. The interested reader may consult Supplemental Material D for further details regarding the derivation. The final state-space realization of the subdomain Ω_{sc} is:

$$\begin{aligned}
\frac{d}{dt} \underbrace{\begin{pmatrix} \bar{u}(t) \\ \bar{p}(t) \\ \bar{\varphi}(t) \end{pmatrix}}_{\underline{X}^{(sc)}(t)} &= \underbrace{\begin{pmatrix} 0 & 0 & 0 \\ 0 & 0 & 0 \\ 0 & -1/\rho_0 & 0 \end{pmatrix}}_{\underline{A}^{(sc)}} \underbrace{\begin{pmatrix} \bar{u}(t) \\ \bar{p}(t) \\ \bar{\varphi}(t) \end{pmatrix}}_{\underline{X}^{(sc)}(t)} \\
+ \underbrace{\begin{pmatrix} 0 & \frac{1}{\rho_0 L_{sc}} & 0 & -\frac{1}{\rho_0 L_{sc}} \\ \frac{2S_1 c_0^2 \rho_0}{L_{sc}(S_1+S_2)} & 0 & \frac{2S_2 c_0^2 \rho_0}{L_{sc}(S_1+S_2)} & 0 \\ 0 & 0 & 0 & 0 \end{pmatrix}}_{\underline{B}^{(sc)}} \underbrace{\begin{pmatrix} u_s^{\Omega_1}(t) \\ p^{\Omega_1}(t) \\ u_s^{\Omega_2}(t) \\ p^{\Omega_2}(t) \end{pmatrix}}_{\underline{U}^{(sc)}(t)} \quad (B.1)
\end{aligned}$$

The state-vector $\underline{X}^{(sc)}(t)$ contains the volume-averaged velocity $\bar{u}(t)$, pressure $\bar{p}(t)$, and acoustic potential $\bar{\varphi}(t) = -\int \bar{p}(t') dt' / \rho_0$. The first two components of the input vector $\underline{U}^{(sc)}(t)$ are imposed by the duct Ω_1 , while the last two are imposed by the duct Ω_2 . We then note $\underline{B}_1^{(sc)}$ (resp. $\underline{B}_2^{(sc)}$) the matrix consisting of the first two columns (resp. last two columns) of $\underline{B}^{(sc)}$. In Eq. (B.1), the first two lines essentially impose acoustic momentum and acoustic volume flux conservation. For low frequencies, these conservation relations reduce to the classical quasi-static jump relations $p^{\Omega_1} = p^{\Omega_2}$ and $S_1 u_s^{\Omega_1} = -S_2 u_s^{\Omega_2}$. The third equation of the dynamical system is a time-integrator that facilitates the computation of the output vector, as the two ducts Ω_1 and Ω_2 require normal acoustic velocity and acoustic potential as inputs. Outputs for the state-space representation of Ω_{sc} are computed thanks to first-order approximations:

$$\underbrace{\begin{pmatrix} u_s(0, t) \\ \varphi(0, t) \\ u_s(L_{sc}, t) \\ \varphi(L_{sc}, t) \end{pmatrix}}_{\underline{Y}^{(sc)}(t)} = \underbrace{\begin{pmatrix} \frac{1}{2}(1 + \frac{S_2}{S_1}) & 0 & 0 \\ 0 & 0 & 1 \\ -\frac{1}{2}(1 + \frac{S_1}{S_2}) & 0 & 0 \\ 0 & 0 & 1 \end{pmatrix}}_{\underline{C}^{(sc)}} \underbrace{\begin{pmatrix} \bar{u}(t) \\ \bar{p}(t) \\ \bar{\varphi}(t) \end{pmatrix}}_{\underline{X}^{(sc)}(t)} \quad (B.2)$$

In Eq. (B.2), the feedthrough matrix \underline{D} is zero. The first two lines are outputs that are to be imposed to the first duct Ω_1 at the connection boundary S_{c1} , while the last two lines are outputs that are to be imposed to the second duct Ω_2 at the connection boundary S_{c2} . We then note $\underline{C}_1^{(sc)}$ (resp. $\underline{C}_2^{(sc)}$) the matrix formed with the first two rows (resp. last two rows) of $\underline{C}^{(sc)}$.

Appendix C. Spurious eigenmodes identification

As mentioned in Section 2.2, the over-completeness of the frame expansion may result in poorly conditioned spurious components of the governing dynamical system (Eq. (12)). It is therefore primordial to distinguish these spurious components from the physically meaningful ones. The interested reader is reported to [52] for further discussion regarding spurious components identification. The simplest method to achieve it is the *brute force* approach: after obtaining the eigenmodes of the full-system

with an expansion of size N , the computation is repeated with a different value of N . Eigenmodes that are very sensitive to the number of DoF are then considered as spurious. However, the over-complete frame expansion presented in Section 2.2 was observed to produce only low energy spurious components. Therefore, a more efficient identification procedure based on an energetic criterion was implemented. This one is described below.

Let us consider an eigenvector $\underline{v} = {}^t(\dots a_1 b_1 \dots a_N b_N \dots)$ of the whole system dynamics matrix \underline{A}^f (see Eq. (14) and Appendix A), where the coefficients a_1, \dots, a_N are the state variables involved in the velocity mode shape in the subdomain Ω_i (they correspond to the time-dependent modal amplitudes $\Gamma_n(t)$), and the coefficients b_1, \dots, b_N are the state variables associated to the pressure mode shape in the subdomain Ω_i (they correspond to the time-dependent modal amplitudes $\tilde{\Gamma}_n(t)$). Then, the eigenmode pressure in the subdomain Ω_i is reconstructed as $\Upsilon_p(\vec{x}) = \sum_n b_n \phi_n(\vec{x}) = {}^t \underline{b} \underline{\phi}(\vec{x})$. The L_2 norm of the full system's eigenmode $\Upsilon_p(\vec{x})$, or equivalently its energy, is given by:

$$\|\Upsilon_p\|_2^2 = \langle \Upsilon_p(\vec{x}), \Upsilon_p(\vec{x}) \rangle = {}^t \underline{b} \langle \underline{\phi}(\vec{x}), {}^t \underline{\phi}(\vec{x}) \rangle \underline{b} = {}^t \underline{b} \underline{\Lambda} \underline{b} \quad (\text{C.1})$$

where $\underline{\Lambda}$ is the Gram matrix of the over-complete frame ($\phi_n(\vec{x})$) for the subdomain Ω_i . Therefore, an eigenmode Υ_p of the whole system has a small energy, say lower than a threshold ε , if and only if:

$$\frac{1}{|\underline{\Lambda}|} |\underline{b}|^2 {}^t \underline{b} \underline{\Lambda} \underline{b} < \varepsilon \quad (\text{C.2})$$

where the left-hand side has been non-dimensionalized by the euclidean norm of the Gram matrix $|\underline{\Lambda}|$, and the euclidean norm of the eigenvector $|\underline{b}|^2$. Eq. (C.2) shows that low energy eigenmodes of the full system are directly related to the poor conditioning of the Gram matrix $\underline{\Lambda}$. Indeed, if an orthogonal basis is used for the modal expansion, $\underline{\Lambda}$ is well-conditioned (it is in fact diagonal), and no eigenmodes can possibly satisfy Eq. (C.2): there is therefore no spurious eigenmodes in this case. On the contrary, if an overcomplete frame is used, $\underline{\Lambda}$ becomes ill-conditioned, and vectors \underline{b} lying in singular regions of the spectrum of the quadratic form associated to $\underline{\Lambda}$ can exist. Those satisfy the relation of Eq. (C.2) and are then considered as spurious eigenmodes. The threshold was empirically fixed to $\varepsilon = 10^{-4}$. However, the procedure showed little sensitivity to this parameter: changing the value of ε to 10^{-5} or 10^{-3} did not affect the modes identified as spurious. This methodology was validated on a number of cases with available reference solutions. It is however not formally proved that it is able to differentiate spurious modes for any given system; if it happens to misidentify those for a particular case, the brute force method should be preferred.

Appendix D. State-space representation for an active flame approximated by a Multi-Pole expansion

For a given active flame, fluctuations of heat release rate $Q(t)$ are governed by the FTF of Eq. (24), and the Multi-Pole expansion approximation of the time-delay $e^{-j\omega\tau}$ (Eq. (25)). Recasting each Pole Base Function into the time-domain leads to the state-space realization of the flame:

$$\frac{d}{dt} \underbrace{\begin{pmatrix} Z_1(t) \\ \dot{Z}_1(t) \\ \vdots \\ Z_{M_{PBF}}(t) \\ \dot{Z}_{M_{PBF}}(t) \end{pmatrix}}_{\underline{X}^{(FTF)}(t)} = \underbrace{\begin{pmatrix} 0 & 1 & & & \\ -\omega_{01}^2 & 2c_1 & & & \\ & & \ddots & & \\ & & & 0 & 1 \\ & & & -\omega_{0M_{PBF}}^2 & 2c_{M_{PBF}} \end{pmatrix}}_{\underline{A}^{(FTF)}} \underbrace{\begin{pmatrix} Z_1(t) \\ \dot{Z}_1(t) \\ \vdots \\ Z_{M_{PBF}}(t) \\ \dot{Z}_{M_{PBF}}(t) \end{pmatrix}}_{\underline{B}^{(FTF)}} + \underbrace{\begin{pmatrix} 0 \\ -1/\bar{u} \\ \vdots \\ 0 \\ -1/\bar{u} \end{pmatrix}}_{\underline{B}^{(FTF)}} \underbrace{\left(u^{(ref)}(t) \right)}_{\underline{U}^{(FTF)}(t)} \quad (\text{D.1})$$

In Eq. (D.1), the flame input vector $\underline{U}^{(FTF)}(t)$ has a single entry, the reference fluctuating speed $u^{(ref)}(t) = u(x_B = \beta L_B, t)$. Note that other formulations including a pressure value as reference are also possible. The state-vector $\underline{X}^{(FTF)}(t)$ contains abstract variables that serve as intermediates in the calculation of heat release rate. The state variable $\dot{Z}_k(t)$ can be interpreted as the proportion of normalized heat release fluctuating at frequencies contained in the band of width $2c_k$ centered around ω_{0k} . This state-space realization is completed by the following output equation:

$$\underbrace{\left(Q(t) \right)}_{\underline{Y}^{(FTF)}(t)} = \underbrace{\begin{pmatrix} 0 & -2\bar{Q}a_1 & \dots & 0 & -2\bar{Q}a_{M_{PBF}} \end{pmatrix}}_{\underline{C}^{(FTF)}} \underbrace{\begin{pmatrix} Z_1(t) \\ \dot{Z}_1(t) \\ \vdots \\ Z_{M_{PBF}}(t) \\ \dot{Z}_{M_{PBF}}(t) \end{pmatrix}}_{\underline{X}^{(FTF)}(t)} \quad (\text{D.2})$$

The flame output vector $\underline{Y}^{(FTF)}(t)$ only comprises the heat release rate $Q(t)$, which is reconstructed from a linear combination of the individual components $\dot{Z}_k(t)$ contained in the state-vector.

Supplementary material

Supplementary material associated with this article can be found, in the online version, at doi:[10.1016/j.combustflame.2019.05.010](https://doi.org/10.1016/j.combustflame.2019.05.010).

References

- [1] J.L. Rayleigh, The explanation of certain acoustical phenomena, *Nature* 18 (1878) 319–321.
- [2] T. Poinsot, Prediction and control of combustion instabilities in real engines, *Proc. Combust. Inst.* 36 (1) (2017) 1–28.
- [3] L. Crocco, Aspects of combustion stability in liquid propellant rocket motors part I: fundamentals. low frequency instability with monopropellants, *J. Am. Rocket Soc.* 21 (6) (1951) 163–178.
- [4] N. Noiray, D. Durox, T. Schuller, S. Candel, A unified framework for nonlinear combustion instability analysis based on the flame describing function, *J. Fluid Mech.* 615 (2008) 139–167.
- [5] F. Nicoud, L. Benoit, C. Sensiau, T. Poinsot, Acoustic modes in combustors with complex impedances and multidimensional active flames, *AIAA J.* 45 (2) (2007) 426–441.
- [6] F. Ni, F. Nicoud, Y. Méry, G. Staffelbach, Including flow-acoustic interactions in the Helmholtz computations of industrial combustors, *AIAA J.* 56 (12) (2018) 4815–4829.
- [7] C.F. Silva, F. Nicoud, T. Schuller, D. Durox, S. Candel, Combining a Helmholtz solver with the flame describing function to assess combustion instability in a premixed swirled combustor, *Combust. Flame* 160 (9) (2013) 1743–1754.
- [8] D. Laera, T. Schuller, K. Prieur, D. Durox, S.M. Camporeale, S. Candel, Flame describing function analysis of spinning and standing modes in an annular combustor and comparison with experiments, *Combust. Flame* 184 (2017) 136–152.

- [9] M. Bauerheim, A. Ndiaye, P. Constantine, S. Moreau, F. Nicoud, Symmetry breaking of azimuthal thermoacoustic modes: the UQ perspective, *J. Fluid Mech.* 789 (2016) 534–566.
- [10] A. Avdonin, S. Jaensch, C.F. Silva, M. Češnovar, W. Polifke, Uncertainty quantification and sensitivity analysis of thermoacoustic stability with non-intrusive polynomial chaos expansion, *Combust. Flame* 189 (2018) 300–310.
- [11] J.G. Aguilar, M.P. Juniper, Adjoint methods for elimination of thermoacoustic oscillations in a model annular combustor via small geometry modifications, *ASME Turbo Expo 2018: Turbomachinery Technical Conference and Exposition*, American Society of Mechanical Engineers, 2018.
- [12] A.P. Dowling, S.R. Stow, Acoustic analysis of gas turbine combustors, *J. Propul. Power* 19 (5) (2003) 751–764.
- [13] J. Li, D. Yang, C. Luzzato, A. Morgans, OSCILOS: the open source combustion instability low order simulator, Imperial College London, 2014. <http://www.oscillos.com>
- [14] J. Li, A.S. Morgans, Time domain simulations of nonlinear thermoacoustic behaviour in a simple combustor using a wave-based approach, *J. Sound Vib.* 346 (2015) 345–360.
- [15] X. Han, J. Li, A.S. Morgans, Prediction of combustion instability limit cycle oscillations by combining flame describing function simulations with a thermoacoustic network model, *Combust. Flame* 162 (10) (2015) 3632–3647.
- [16] P.L. Rijke, Notice of a new method of causing a vibration of the air contained in a tube open at both ends, *Lond. Edinb. Dublin Philos. Mag. J. Sci.* 17 (116) (1859) 419–422.
- [17] M. Bauerheim, J.F. Parmentier, P. Salas, F. Nicoud, T. Poinso, An analytical model for azimuthal thermoacoustic modes in an annular chamber fed by an annular plenum, *Combust. Flame* 161 (5) (2014) 1374–1389, doi:10.1016/j.combustflame.2013.11.014.
- [18] M. Bauerheim, M. Cazalens, T. Poinso, A theoretical study of mean azimuthal flow and asymmetry effects on thermo-acoustic modes in annular combustors, *Proc. Combust. Inst.* 35 (3) (2015) 3219–3227.
- [19] P.M. Morse, K.U. Ingard, *Theoretical acoustics*, Princeton University Press, 1968.
- [20] B.T. Zin, M.E. Lores, Application of the Galerkin method in the solution of non-linear axial combustion instability problems in liquid rockets, *Combust. Sci. Technol.* 4 (1) (1971) 269–278.
- [21] F. Culick, Nonlinear behavior of acoustic waves in combustion chambers – II, *Acta Astronaut.* 3 (9–10) (1976) 735–757.
- [22] F.E.C. Culick, Combustion instabilities in liquid-fueled propulsion systems: an overview, *AGARD Conference Proceedings 450*, Belgium: NATO ASI Series Publication Coordination Office (1989).
- [23] F.E. Culick, V. Yang, Overview of combustion instabilities in liquid-propellant rocket engines, *Liq. Rocket Engine Combust. Instab.* 169 (1995) 3–37.
- [24] F. Culick, Unsteady motions in combustion chambers for propulsion systems, *NATO Research and Technology Organization*, 2006. No. AC/323 (AVT-039) TP/10.
- [25] M.P. Juniper, Triggering in the horizontal Rijke tube: non-normality, transient growth and bypass transition, *J. Fluid Mech.* 667 (2011) 272–308.
- [26] I.C. Waugh, M.P. Juniper, Triggering in a thermoacoustic system with stochastic noise, *Int. J. Spray Combust. Dyn.* 3 (3) (2011) 225–242.
- [27] K. Balasubramanian, R.I. Sujith, Non-normality and nonlinearity in combustion-acoustic interaction in diffusion flames, *J. Fluid Mech.* 594 (2008) (2008) 29–57.
- [28] N. Noiray, M. Bothien, B. Schuermans, Investigation of azimuthal staging concepts in annular gas turbines, *Combust. Theory Model.* 15 (5) (2011) 585–606.
- [29] N. Noiray, B. Schuermans, Deterministic quantities characterizing noise driven Hopf bifurcations in gas turbine combustors, *Int. J. Non-Linear Mech.* 50 (2013) 152–163.
- [30] N. Noiray, B. Schuermans, On the dynamic nature of azimuthal thermoacoustic modes in annular gas turbine combustion chambers, *Proc. R. Soc. A* 469 (2013) 20120535.
- [31] G. Ghirardo, M.P. Juniper, J.P. Moeck, Weakly nonlinear analysis of thermoacoustic instabilities in annular combustors, *J. Fluid Mech.* 805 (2016) 52–87.
- [32] S.R. Stow, A.P. Dowling, A time-domain network model for nonlinear thermoacoustic oscillations, *J. Eng. Gas Turb. Power* 131 (3) (2009) 031502.
- [33] B. Schuermans, V. Bellucci, C.O. Paschereit, Thermoacoustic modeling and control of multi burner combustion systems, *ASME Turbo Expo 2003*, Collocated with the 2003 International Joint Power Generation Conference, American Society of Mechanical Engineers (2003), pp. 509–519.
- [34] B. Schuermans, Modeling and control of thermoacoustic instabilities, Ph.D. thesis, EPFL, 2003.
- [35] V. Bellucci, B. Schuermans, D. Nowak, P. Flohr, C.O. Paschereit, Thermoacoustic modeling of a gas turbine combustor equipped with acoustic dampers, *ASME Turbo Expo 2004: Power for Land, Sea, and Air*, American Society of Mechanical Engineers (2004), pp. 635–644.
- [36] S. Bethke, U. Wever, W. Krebs, Stability analysis of gas-turbine combustion chamber, 11th AIAA/CEAS Aeroacoustics Conference (2005), p. 2831.
- [37] S. Evesque, W. Polifke, Low-order acoustic modelling for annular combustors: validation and inclusion of modal coupling, *ASME Turbo Expo 2002: Power for Land, Sea, and Air*, American Society of Mechanical Engineers (2002), pp. 321–331.
- [38] A. Orchini, G.A. Mensah, J.P. Moeck, Effects of nonlinear modal interactions on the thermoacoustic stability of annular combustors, *J. Eng. Gas Turb. Power* 141 (2) (2019) 021002.
- [39] Y. Dong, A.S. Morgans, Low-order network modeling for annular combustors exhibiting longitudinal and circumferential modes, *ASME Turbo Expo 2018*, Paper no. GT2018-76506 (2018), pp. 1–12.
- [40] T. Sayadi, V. Le Chenadec, P.J. Schmid, F. Richecoeur, M. Massot, Thermoacoustic instability – a dynamical system and time domain analysis, *J. Fluid Mech.* 753 (2014) 448–471.
- [41] T. Emmert, M. Meindl, S. Jaensch, W. Polifke, Linear state space interconnect modeling of acoustic systems, *Acta Acust. United Acust.* 102 (5) (2016) 824–833.
- [42] G. Ghirardo, M.P. Juniper, M.R. Bothien, The effect of the flame phase on thermoacoustic instabilities, *Combust. Flame* 187 (2018) 165–184.
- [43] P.M. Morse, H. Feshbach, *Methods of theoretical physics*, Technology Press, 1946.
- [44] I. Daubechies, A. Grossmann, Y. Meyer, Painless nonorthogonal expansions, *J. Math. Phys.* 27 (5) (1986) 1271–1283.
- [45] R.M. Young, *An introduction to non-harmonic fourier series*, 93, Revised edition, Elsevier, 2001.
- [46] B. Friedland, *Control system design: an introduction to state-space methods*, Courier Corporation, 2012.
- [47] R. Redheffer, On a certain linear fractional transformation, *Stud. Appl. Math.* 39 (1–4) (1960) 269–286.
- [48] P. Subramanian, R.S. Blumenthal, W. Polifke, R. Sujith, Distributed time lag response functions for the modelling of combustion dynamics, *Combust. Theory Model.* 19 (2) (2015) 223–237.
- [49] Q. Douasbin, C. Scalo, L. Selle, T. Poinso, Delayed-time domain impedance boundary conditions (D-TDIBC), *J. Comput. Phys.* 371 (2018) 50–66.
- [50] G. Ghirardo, B. Čosić, M.P. Juniper, J.P. Moeck, State-space realization of a describing function, *Nonlinear Dyn.* 82 (1–2) (2015) 9–28.
- [51] M. Meindl, T. Emmert, W. Polifke, Efficient calculation of thermoacoustic modes utilizing state-space models, 23rd International Congress on Sound and Vibration, ICSV23, Athens, Greece, 2016.
- [52] J.P. Boyd, *Chebyshev and Fourier spectral methods*, Courier Corporation, 2001.